

1 **Hydrothermal alteration of the Ediacaran Volyn-Brest volcanics on the western margin**  
2 **of the East European Craton**

3

4 JAN ŚRODOŃ<sup>1\*</sup>, OKSANA KUZMENKOVA<sup>2</sup>, JAN J. STANEK<sup>3</sup>, SABINE PETIT<sup>4</sup>, DANIEL BEAUFORT<sup>4</sup>,  
5 H. ALBERT GILG<sup>5</sup>, SIRLE LIIVAMÄGI<sup>1</sup>, MAGDALENA GORYL<sup>6</sup>, LESZEK MARYNOWSKI<sup>6</sup>, MAREK  
6 SZCZERBA<sup>1</sup>

7

8 <sup>1</sup>Institute of Geological Sciences, Polish Academy of Sciences, Krakow, Poland

9 (\*corresponding author: [ndsrodon@cyf-kr.edu.pl](mailto:ndsrodon@cyf-kr.edu.pl))

10 <sup>2</sup>Research and Production Center for Geology, Minsk, Belarus

11 <sup>3</sup>Institute of Physics, Jagiellonian University, Krakow, Poland

12 <sup>4</sup>Institut de Chimie des Milieux et Matériaux de Poitiers, Univ. Poitiers - CNRS, France

13 <sup>5</sup>Engineering Geology, Technical University of Munich, Munich, Germany

14 <sup>6</sup>University of Silesia, Faculty of Earth Sciences, Sosnowiec, Poland

15

16 **Abstract**

17

18 The Ediacaran continental flood basalts and associated tuffs were studied to identify and  
19 quantify alteration processes by means of XRD and chemistry, supplemented by Mössbauer  
20 and FTIR spectroscopies, petrography, oxygen and iron isotopes, K-Ar dating, and organic  
21 geochemistry. Two superimposed alteration processes were identified: the Ediacaran  
22 hydrothermal alteration, induced by meteoric waters, heated and put in motion by the cooling  
23 basalt, and the Caledonian and/or Variscan potassic alteration. The degree of basalt alteration  
24 was quantified using as an index the sum of primary minerals in the bulk rock. The sequence  
25 of minerals dissolved and crystallized during the hydrothermal alteration was established. The  
26 alteration resulted in the loss of Ca (dissolution of plagioclases), compensated by the gain of

27 water and Mg (crystallization of clays), and proceeded from the edges of the basalt flows in  
28 an oxidizing environment, evidenced by the increasing amount of hematite and  $\text{Fe}^{3+}/\text{Fe}^{2+}$  ratio  
29 of the bulk rock. Cyanobacteria were active in the hydrothermal system, most probably  
30 responsible for the measured negative  $\delta^{56}\text{Fe}$  values and more reducing conditions at the stage  
31 of intense alteration. Chlorophaeite (palagonite), following quartz as the earliest  
32 petrographically identifiable basalt alteration product was found to vary systematically from  
33 fully isotropic to birefringent. The chlorophaeite was identified as a mixture of Fe-  
34 montmorillonite and Fe-saponite, identical with griffithite and oxysmectites, probably  
35 preceded by a finer-grained ferrosaponite at the isotropic stage. REE content of chlorophaeite  
36 indicates basaltic volcanic glass (sideromelane) as the major source of material. REE in clays  
37 are contained mostly in the dioctahedral smectite, while in the bulk rock mostly in  
38 phosphates. The smectite characteristics and Mg enrichment are indicative of the  
39 hydrothermal basalt alteration process, which perhaps was dominant also on Mars.

40 Both mineral and chemical composition of tuffs vary continuously from basaltic to  
41 felsic, the latter close to the measured rhyodacite composition, dominated by quartz and  
42 feldspars. The basaltic tuffs resemble the most altered basalts but contain also abundant albite  
43 and chlorite, indicative of higher alteration temperatures, up to 220°C. Tuff composition  
44 indicates stronger component of felsic volcanism in the trap formation than evidenced by the  
45 preserved bodies of effusive rocks.

46 **Key words:** aluminoceladonite; chlorophaeite; cyanobacteria; griffithite; ferrosaponite;  
47 Martian smectite, palagonite.

48

49 **Introduction**

50

51 Sub-surface (non-related to weathering) alteration of basalts is a widespread and intensely  
52 studied phenomenon, known from three major Earth environments: submarine hydrothermal,  
53 burial diagenetic/metamorphic, and continental hydrothermal.

54 A good example of submarine hydrothermal alteration within a 60-165°C measured  
55 temperature range is the 1300 m profile of DSDP Hole 504B south of the Costa Rica Rift in  
56 the Pacific (Alt et al., 1986; Shau and Peacor, 1992). A clear alteration sequence was  
57 observed: iron oxides, saponite, celadonite, phillipsite, anhydrite, and aragonite formed below  
58 150°C, and mixed-layer saponite-chlorite, corrensite, corrensite/chlorite, and finally chlorite,  
59 minor talc, quartz, pyrite, epidote, laumontite, heulandite, prehnite, actinolite, and albite  
60 formed in deeper, hotter parts. Altered basalt becomes a sink for Mg and K from seawater,  
61 affecting the element mass balance of the oceans. From the saponitic to chloritic end of the  
62 trioctahedral clay sequence, Si/(Si+Al) ratio decreases, while Fe/(Mg+Fe) increases. In  
63 another submarine site (801), Alt et al. (1992) observed a range of alteration products from  
64 pure saponite to almost pure dioctahedral smectite, accompanied by pyrite and calcite. Other  
65 samples contain celadonite, glauconite, and iron oxides. With progressing alteration  
66 (measured by  $H_2O^+$ ), an increase in  $\delta^{18}O$ , iron oxidation and  $K_2O$  is observed, while CaO  
67 decreases, but MgO does not show a clear trend.

68 A particularly clear sequence of burial metamorphic alteration zones was documented  
69 (Schmidt, 1993; Schmidt and Robinson, 1997) from the 8 km thick pile of the Keweenawan  
70 Middle Proterozoic continental subaerial rift basalts, outcropping on the shore of Lake  
71 Superior, and known for native copper deposits. At the top of sequence, saponite is dominant,  
72 and going down section, random chlorite-smectite and corrensite appear, accompanied by  
73 laumontite and albite, then chlorite with prehnite and pumpellyite, and finally epidote and  
74 actinolite (greenschist facies). Albite is the most abundant alteration product of Ca-rich  
75 plagioclase. Fe oxides were not reported. Celadonite occurs sporadically. Like in the

76 submarine alteration, from the saponitic to chloritic end of the trioctahedral clay sequence  
77 Si/(Si+Al) ratio decreases, while Fe/(Mg+Fe) increases. Strong control of porosity and  
78 permeability over the extent of alteration is evident: massive flow centres have less advanced  
79 alteration than porous, thus permeable tops and bottoms.

80 Subaerial hydrothermal alteration of basalts has been most thoroughly studied in  
81 Iceland, where data measured in active hydrothermal systems were used to assess temperature  
82 ranges of subsequent alteration zones, analogous to burial and marine hydrothermal (Franzson  
83 et al., 2008): smectite+zeolites correspond to the 50-200°C range, trioctahedral mixed layer  
84 clays dominate over the 200-220°C range, then chlorite takes over and albitization starts,  
85 epidote appears at ca. 240°C, actinolite at 275°C, and amphibole above 350°C. Analogous  
86 basalt alteration sequences have been identified in other hydrothermal fields, e.g. in a  
87 geothermal well in Hawaii (Stone and Fan, 1978).

88 This review demonstrates that the alteration of basalts in three different environments  
89 proceeds via a very similar sequence of mineral assemblages, which indicates dominant  
90 control of the rock chemistry over the alteration mineralogy, with porosity and permeability  
91 affecting the reaction progress, and in particular the pathway of smectite to chlorite transition  
92 (Robinson et al., 2002).

93 Similar qualitative mineralogical data (e.g. Juskowiakowa, 1974; Kuzmenkova, 2005;  
94 Derevska et al., 2006; Emetz et al., 2006; Kuzmenkova et al., 2006; Melnychuk, 2006;  
95 Shumlyanskyy and Tsymbal, 2006; Skakun et al., 2006) are available also for the Ediacaran  
96 Volyn-Brest volcanics of the East European Craton (EEC; Figure 1) and they inspired the  
97 present study. Our study was focused on adding a quantitative mineralogical dimension to the  
98 knowledge of hydrothermal basalt alteration, on understanding the conditions of this  
99 alteration, and on discriminating the effects of younger alteration phenomena. The clay  
100 alteration products were studied in most detail to characterize the substrate on which the

101 Ediacaran weathering of basalts took place (Liivamägi et al., 2018). It was also hoped that  
102 better understanding of the Ediacaran basalt hydrothermal alteration may be useful as a model  
103 for the origin of clays on Mars. They have been detected both by remote and in-situ methods  
104 as the main products of basalt alteration in the Noachian age (e.g., Ehlmann et al., 2011a,b;  
105 Carter et al., 2013; Chemtob et al., 2015). The origin of these clay minerals is currently  
106 debated, and potential formation environments include subsurface hydrothermal systems,  
107 subaerial weathering profiles, lacustrine environments, and steam or a supercritical  
108 atmosphere of water and CO<sub>2</sub> (e.g., Ehlmann et al., 2011a,b; Vaniman et al., 2014; Bishop et  
109 al., 2018; Cannon et al., 2018). Here, we identify mineralogical and geochemical signatures of  
110 subsurface hydrothermal clay deposits that can be used to constrain clay formation  
111 environments on Mars.

112

### 113 **Study area**

114

115 The Volyn-Brest Ediacaran flood basalts, up to 500 m of lavas and volcanoclastics, cover  
116 140, 000 km<sup>2</sup> of the western margin of the East European Craton. The original volcanic cover  
117 extended much further east and north, as evidenced by isolated erosional remnants in these  
118 areas (Figure 1). Towards the southeast, the volcanic cover continues to an unknown distance,  
119 deeply buried below Paleozoic sediments of the Teisseyre-Tornquist Zone (Paczeńska, 2010),  
120 which separates the Precambrian from the Paleozoic platform. In Volyn (northwest Ukraine  
121 north of Lvov), the Ediacaran basalts occur over ca. 80 km<sup>2</sup> at the surface or under a thin  
122 cover of the Cretaceous rocks and have been used as building stones since XVII century  
123 (Rajchel, 2012). In other regions, they are covered by the Late Ediacaran clastic sediments  
124 and younger deposits.

125           The Volyn-Brest trap region is a continental flood basalt province, analogous to the  
126 well- known Columbia River, Deccan, Paraná, or Siberian traps (Kuzmenkova et al., 2010). It  
127 is considered a product of the supercontinent Rodinia rifting, which detached Amazonia from  
128 Baltica by opening of the Tornquist Ocean in the Late Ediacaran (Poprawa et al., 1999;  
129 Nawrocki and Poprawa, 2006). Deep root bodies of the basalt province were identified  
130 recently by geophysical methods in the Teisseyre-Tornquist Zone, SE of Brest (Mazur et al.,  
131 2018a).

132           Volyn basalts have been studied since the mid-19th century, and particular interest  
133 was generated by finding a native copper mineralization (Małkowski, 1929). These early  
134 studies (conf. Białowska et al., 2002 for references) were carried out on rocks from the  
135 Volyn outcrops, later also on the core materials from Belarus, Poland and Ukraine (Ushakova,  
136 1962; Juskowiak and Ryka, 1967; Makhnach and Veretennikov, 1970; Juskowiakowa, 1971;  
137 Compston et al., 1995; Białowska et al., 2002; Bakun-Czubarow et al., 2002; Emetz et al.,  
138 2004; Kuzmenkova, 2007; Nosova et al., 2008; Kuzmenkova, 2011; and many others).  
139 Recent investigations, summarized in a monograph (Shumlyanskyy, ed., 2006), were centered  
140 on the genesis of native copper mineralization. All of these studies were devoted mainly to  
141 geochronology, geochemistry, and petrographic observations of mineral successions.

142           Shumlyanskyy et al. (2016) reviewed the geochronological literature. Early K-Ar  
143 measurements of the whole rock gave a broad range of 690-540 Ma. The  $^{40}\text{Ar}/^{39}\text{Ar}$  whole  
144 rock method yielded two age groups: 590-560 Ma (magma crystallization) and 393-369 Ma  
145 (potassic alteration). The Rb-Sr isochron method applied to four whole rock samples gave an  
146 imprecise age of  $552\pm 59$  Ma, while U-Pb zircon ages range from  $551\pm 4$  Ma to  $573\pm 14$  Ma.

147           Geochemical studies identified the trap rocks as within plate continental basalts and  
148 documented vertical zonation of the trap: picobasalts and subalkaline olivine basalts in the  
149 lower basalt flows are covered locally (Figure 1) by felsic rocks (andesite, dacite, rhyodacite,

150 trachyandesite), and tholeiites dominate the upper flows, all accompanied by more or less  
151 abundant tuffs (Bakun-Czubarow et al., 2002; Kuzmenkova et al., 2008; Nosova et al., 2008).  
152 The Ediacaran paleosols are developed both on the lower (Kuzmenkova et al., 2011) and on  
153 the upper basalts (Levykh, 1999; Liivamägi et al., 2018), documenting the continental,  
154 subaerial origin of the volcanic sequence.

155         Since the findings of native copper (Małkowski, 1929) and celadonite (Kamieński,  
156 1929), later confirmed by Lazarenko (1956), it was realized that Volyn basalts underwent  
157 widespread hydrothermal alteration of variable intensity. Shumlyanskyy and Tsymbal (2006)  
158 recognized this variable degree of alteration and characterized geochemically the alteration  
159 sequence: oxidation of iron; increase of MgO, K<sub>2</sub>O, LOI, Rb, Ba, Zr, Nb, Ta, Th, U; decrease  
160 of CaO and Sr. They observed more intense alteration of tuffs compared to the flood basalts,  
161 but they interpreted the exceptionally high MgO content of some tuffs as reflecting the  
162 primary volcanic composition. Melnychuk (2006) documented carbonate, zeolite, and  
163 prehnite-pumpellyite zones of hydrothermal alteration in the flood basalts and volcanic tuffs.

164         In Volyn and Belarus, i.e. outside the Teisseyre-Tornquist Zone, the basalts have  
165 never been deeply buried, as indicated by regional organic geochemistry data for overlying  
166 sediments (Nehring-Lefeld et al., 1977) and confirmed recently by studying the Ediacaran  
167 paleosols developed on basalts (Liivamägi et al., 2018) and hopane biomarkers in the  
168 overlying Ediacaran sediments (Goryl et al., 2018). Initially, a "fresh" appearance of the  
169 unaltered sections was used as evidence of the lack of regional metamorphic or advanced  
170 diagenetic changes (Ushakova, 1962; Juskowiak and Ryka, 1967; Makhnach and  
171 Veretennikov, 1970). Juskowiakowa (1974) observed that the alteration develops from the  
172 upper and lower surfaces of the lava flows, it may be complete in thin flows and tuffs or  
173 tectonic zones, and it involves the development of chlorite, illite and celadonite. The  
174 alteration sequence was characterized by the microscopic studies of Volyn native Cu deposits

175 (Derevska et al., 2006; Emetz et al., 2006; Skakun et al., 2006). Plagioclase (andesine-  
176 anorthite), clinopyroxene, magnetite, ilmenite, titanomagnetite, volcanic glass, and rare  
177 olivine (often recognized only as prehnite pseudomorphs) were identified as primary basaltic  
178 components. Clinocllore, hematite, albite, and pumpellyite were identified as pre-ore  
179 minerals; prehnite, laumontite, wairakite, quartz, and K-spar as syn-ore minerals; and quartz,  
180 stilbite, mordenite, heulandite, thomsonite, tri- and dioctahedral smectite, chlorite,  
181 vermiculite, calcite, analcime, barite, and kaolinite as post-ore minerals. Similar composition,  
182 including a wider range of zeolite minerals, was reported by Kuzmenkova (2005).  
183 Kuzmenkova et al. (2006) characterized in detail glassy-looking accumulations of dark  
184 material, described from various basalts under the name "chlorophaeite" and present even in  
185 very fresh-looking basalts – the equivalent of palagonite (conf. review by Stroncik and  
186 Schmincke, 2002), of the late-magmatic lithogel of Simanovich et al. (1986), and probably of  
187 glass of Emetz et al. (2006). Smectite, chlorite and analcime were identified in chlorophaeite  
188 accumulations. Mysiak et al. (2016) reported native Cu and Ag occurring along with  
189 hydrothermal minerals, while native Fe, Sn, Al, chlorides of Sn and Fe, and a FeCrNiTi alloy  
190 in pneumatolytic veins cutting the hydrothermal alteration zones. Native Fe was reported also  
191 by Kvasnytsya et al. (2006).

192 Kuzmenkova (2007) investigated the felsic rocks (rhyodacites) and found large  
193 amounts of quartz, K-spar, albitized plagioclase, and chlorite+biotite pseudomorphs after  
194 pyroxene. The chemical composition of tuffs is also much more variable than flood basalts,  
195 demonstrating higher K and Na and lower Ca. Saponite, mixed-layer chlorite-smectite,  
196 hydromica, analcime, other zeolites, and hematite were identified as alteration minerals in the  
197 tuffs.

198 To summarize: the Volyn flood basalt mineral and chemical composition, and their  
199 alteration processes have been well recognized by numerous studies. This study aims at

200 quantifying the alteration process, investigating its relationship to the conditions on the  
201 Ediacaran land, and investigating in more detail the iron-rich smectite, which is the main  
202 alteration product.

203

## 204 **Materials**

205

206 All investigated samples (locations in Figure 1) are core materials, except for the Tashki  
207 samples, collected from a quarry. Present depth, macroscopic characteristics, and location of a  
208 sample in the trap profile (lower, middle, and upper volcanogenic strata) are given if available  
209 in Inline Supplementary Tables 1 and 2, listing separately flood basalts, clays from veins and  
210 cavities in basalts, felsic rocks, and tuffs, according to the macroscopic identification. Several  
211 chlorophaeite accumulations, studied earlier by Kuzmenkova et al. (2006) were also  
212 investigated, some of them only by FTIR because of small amount of the available material,  
213 along with the reference montmorillonite samples 4529-2 and 4517-1 from the paleosol,  
214 developed on the Volynian basalt (Liivamägi et al., 2018). In three cases (Mokrany-1, 2, and  
215 3), both basalt sample and a chlorophaeite accumulation separated from this basalt sample  
216 were available. Additional paleosol samples were used in the organic geochemistry study.

217

## 218 **Methods**

219

220 The main techniques used in this study are: quantitative X-ray diffraction of the bulk rock  
221 (QXRD) using in-house Q-Min software (by Dr. M. Szczerba, Institute of Geological  
222 Sciences PAS), XRD of the clay fractions separated from the bulk rock, chemical analysis  
223 (major elements by X-Ray Fluorescence (XRF) and trace elements (including REE) by Laser  
224 Ablation Inductively Coupled Plasma Mass Spectrometry (LA-ICP-MS) on the same lithium

225 borate fused disc), Mössbauer spectroscopy and iron isotope composition of the bulk rock and  
226 of the clay fractions, and the K-Ar dating of clay fractions. These methods are identical to  
227 those used by Liivamägi et al. (2018) in the study of paleosols developed on these basalts, and  
228 their descriptions are reproduced with some modifications in the Supplementary Materials,  
229 along with additional techniques applied in this study: oxygen isotope and FTIR  
230 measurements of the bulk rock and the clay fraction, organic geochemistry, and petrographic  
231 observations of the basalt alteration products.

## 232 **Results**

233

### 234 ***XRD of the bulk rock***

235

#### 236 ***Flood basalts and chlorophaeites***

237 Quantitative XRD data for basalts (in wt%) are given in Inline Supplementary Table 1, and  
238 representative XRD patterns, illustrating the encountered variability of mineral composition,  
239 are presented in Figure 2. Most common major components are calcic plagioclase, pyroxene,  
240 magnetite, dioctahedral smectite, trioctahedral smectite and chlorite or mixed-layer chlorite-  
241 smectite. Quantities of these major components vary broadly. Both di- and trioctahedral  
242 smectites are present in most samples, as evidenced by separate 02 and 06 peaks (Figure 2).  
243 Common minor components are: quartz, potassium feldspar of orthoclase/sanidine/sanidine  
244 group (most often more abundant than quartz), and hematite. Orthoclase cannot be  
245 distinguished from sanidine in the bulk rock XRD, so they are reported as a group. Rare  
246 minor components are ilmenite, anatase, analcime, pseudobrookite, clinoptilolite, laumontite,  
247 calcite, and siderite. Olivine, reported in published petrographic studies, was not detected.  
248 The mineral compositions of two available gabbro samples fall within the limits characteristic  
249 of basalts (Inline Supplementary Table 1). Three chlorophaeite accumulations were

250 investigated by XRD along with the host basalts, but only qualitatively in glass capillaries,  
251 because of the small amount of sample available. Di- and trioctahedral smectites, quartz and  
252 traces of calcic plagioclase, calcite and dolomite were detected in these samples. The  
253 smectitic clays are identified as separate di- and trioctahedral phases based on well resolved  
254 02 reflections, by analogy to the bulk basalt XRD patterns, where the 06 reflections could also  
255 be recorded (compare Figures 2 and 3).

256

### 257 **Felsic rocks**

258 Three rhyodacite samples were available. Their mineral composition is totally different from  
259 basalts: quartz, orthoclase/sanidine/sanidine, dioctahedral clay (illite-smectite), trioctahedral  
260 mica, hematite, chlorite, and a trace of kaolinite in one sample (Inline Supplementary Table 1,  
261 Inline Supplementary Figure 1).

262

### 263 **Tuffs**

264 Only purevolcanic materials were considered (Inline Supplementary Table 2, Inline  
265 Supplementary Figure 1). The presence of minerals absent from pyroclastic materials:  
266 microcline and muscovite was regarded as evidence of non-volcanic contamination (tuffites)  
267 and such samples were not included in the analysis. Mineral composition of tuffs is extremely  
268 variable. Most common components are: quartz, orthoclase/sanidine, Ca-plagioclase,  
269 dioctahedral expandable clay (illite-smectite or smectite), aluminoceladonite (identified by  
270  $1M_{IV}$  polytype and  $d_{001}$  close to  $9.88 \text{ \AA}$ , characteristic of this mineral, and distinguishing it  
271 from celadonite of  $d_{001}=9.97 \text{ \AA}$ ), and chlorite or mixed-layer chlorite-smectite. Less abundant  
272 are trioctahedral smectite, albite, anatase, hematite, analcime, minor and rare are pyroxene  
273 and amphibole. Locally, tuffs contain dolomite, Mn-Fe dolomite and calcite (Pinsk-26), or  
274 only calcite (Tashki).

275

276 **Tuff-basalt alternation**

277 The contrasting characteristics of flood basalts and tuffs, emerging from the entire data set,  
278 can be observed also in a single vertical profile (Kobryn), composed of three basalt flows  
279 interbedded with four tuff layers free of non-volcanic contamination (Inline Supplementary  
280 Table 2). Flood basalts contain trace of quartz and hematite, abundant Ca-plagioclase,  
281 pyroxene, and trioctahedral smectite, and occasional minor chlorite or chlorite-smectite. Clay  
282 abundances increase towards the top surfaces of the basalt flows. Tuffs contain abundant  
283 quartz, orthoclase/sanidine, Ca-plagioclase and hematite, chlorite plus minor chlorite-  
284 smectite, dioctahedral illite-smectite, and aluminoceladonite. Top samples from two tuff  
285 layers contain kaolinite.

286

287 ***XRD identification of clay fractions***

288

289 Mineral composition of <0.2  $\mu\text{m}$  clay fractions, including percent smectite (%S) in mixed-  
290 layer illite-smectite, measured from the diagnostic peak positions on the glycolated patterns,  
291 using the regressions based on data of Środoń et al. (2009), is presented in Inline  
292 Supplementary Table 3.

293

294 **Flood basalts**

295 Attempts to separate pure clay fractions were unsuccessful for basalts with >60% of primary  
296 minerals, despite long grinding in McCrone mill and sonification. The <0.2  $\mu\text{m}$  separates  
297 contain abundant plagioclase and exhibit poor orientation (Mokransy-1B in Inline  
298 Supplementary Figure 2), indicating intimate intergrowth of smectite with host plagioclase  
299 crystals. More altered samples allow clean separation of clay fractions (e.g. 4504-1A in Inline

300 Supplementary Figure 2), which contain mixtures of di- and trioctahedral smectites (Inline  
301 Supplementary Figure 3), as evidenced by separate 02 and 06 reflections. Sample 4417-1  
302 (Inline Supplementary Figure 2) contains corrensite, chlorite and illite-smectite with ca. 40%  
303 S. Among clays filling cavities in basalts, pure trioctahedral minerals were identified: saponite  
304 (4600-1), and chlorite with minor corrensite (Kob-23: both shown in Inline Supplementary  
305 Figure 2). Sample 4600-1 contains a minor admixture of corrensite in 2-0.2  $\mu\text{m}$  fraction.

306

### 307 **Tuffs**

308 Clay fractions of tuffs differ from flood basalts by the presence of aluminoceladonite in many  
309 samples: from a trace to the dominant component. The trace amounts are associated with  
310 illite-smectite of >70%S (Inline Supplementary Figure 4: Pinsk-40), sometimes also with  
311 small amounts of chlorite-smectite close to corrensite (Inline Supplementary Figure 4:  
312 Tashki-10), and characterize rocks with low quartz content (<10%). In one sample a chlorite-  
313 smectite close to chlorite was dominant (Inline Supplementary Figure 4: Pinsk-40C).

314 Samples with more abundant aluminoceladonite contain illite-smectite of <50 %S,  
315 chlorite-smectite close to corrensite, discrete chlorite, and represent rocks with higher quartz  
316 content (>10%, Inline Supplementary Figure 4: Pinsk-46). Such samples contain abundant  
317 chlorite in 0.2-2  $\mu\text{m}$  fraction. Most commonly, the 005 reflection of aluminoceladonite is at  
318  $1.978\text{\AA}$  ( $d_{001}=9.90\text{\AA}$ ). In the extreme case, aluminoceladonite is the dominant component,  
319 (Inline Supplementary Figure 4: Kob-9B). In this sample, aluminoceladonite is accompanied  
320 by a regular illite, as 005 and 003 reflections are split into two peaks.

321

### 322 ***Chemical data***

323

324 The chemical data were obtained for selected bulk samples and clay fractions (Inline  
325 Supplementary Table 4). The bulk rock data are grouped according to lithology into five  
326 categories: flood basalts, rhyodacites, tuffs, chlorophaeite, and vein and cavity clays. When  
327 average values are compared, tuffs are intermediate between flood basalts and rhyodacites,  
328 except Mg is similar to that of basalt and tuffs have elevated LOI, B, Cr, Cs, Cu, Ni, and Pb.  
329 The chlorophaeite sample (Mokransy-3A), when compared to its host basalt (Mokransy-3B), is  
330 depleted in most elements, including HREE and Fe, Na, Ca, Ba, Sr, Nb, Sc, Y, Zn, U, V, and  
331 Zr, but is strongly elevated in Si and moderately elevated in Mg, LOI, Cr, Cs, Cu, Ni, Rb, and  
332 LREE. The vein clays, when compared to average basalt, have strongly elevated Mg, LOI,  
333 and Co, elevated Fe, Ga and Ni, but most of the elements are depleted. REE are depleted  
334 particularly strongly and several times stronger in chlorite (Kob-23) than in the trioctahedral  
335 smectite sample (4600-1). The clay fraction of the latter is depleted even stronger. When clay  
336 fractions separated from basalts are compared to their host rocks, the common characteristics  
337 are the clay enrichment in Mg, LOI, Be, Co, Cr, Mo, and Ni, and depletion in B, K, Ca, Sr,  
338 Ba, Ti, Cu, Nb, and V. REE contents of the basalt clay fractions do not differ significantly  
339 from the bulk rock contents.

340

#### 341 *Mössbauer data*

342

343 The Mössbauer data (Table 1) were collected for a range of bulk rock basalt, vein clay, and  
344 tuff samples, selected clay fractions <0.2 µm, and two pyroxenes separated from the basalts.  
345 The spectra of pure minerals separated from basalts were used as starting parameters for  
346 fitting polymineral spectra of rocks (Table 1, Figure 4) and include: trioctahedral smectite  
347 (Inline Supplementary Figure 5, 4600-1), dioctahedral smectite (4529-2, cf. Liivamägi et al.,

348 2018), chlorite (Figure 4, Kob-23), and pyroxenes (4519-0 and 4603-1). Where applicable,  
349 the well known sextet of hematite and two sextets of magnetite were included in the fit.

350 Chlorite was found to contain only  $\text{Fe}^{2+}$ , dioctahedral smectite only  $\text{Fe}^{3+}$ , and  
351 trioctahedral smectite both  $\text{Fe}^{2+}$  and  $\text{Fe}^{3+}$ . Two pyroxenes contained  $\text{Fe}^{2+}$  distributed over two  
352 possible crystallographic positions in different proportions, visible in the Mössbauer spectra  
353 as two well resolved quadrupole doublets. Finally, the rocks were analyzed assuming up to 7  
354 different components with 9 subspectra (Table 1, Figure 4). In sample Mokraný-1B one  
355 additional component was detected with parameters characteristic of the amorphous wüstite,  
356  $\text{FeO}$ .

357 The measured bulk rock percent  $\text{Fe}^{2+}$  in the total Fe vary from 65 to 23% for flood  
358 basalts and from 49 to 11% for tuffs. The corresponding  $\text{Fe}^{2+}$  values, calculated for the clay  
359 fraction from the bulk rock data, are lower than the bulk rock values for less altered flood  
360 basalts but higher than the bulk rock values for more altered basalts and tuffs. The %  $\text{Fe}^{2+}$   
361 values of clays, measured for the  $<0.2 \mu\text{m}$  fractions and calculated from the bulk rock analysis  
362 are essentially identical, if no chlorite or chlorite-smectite is present (Mokraný-3B and 4504-1  
363 in Table 1), indicating that the separation procedure did not affect the oxidation status of Fe in  
364 smectites. The %  $\text{Fe}^{2+}$  values are lower in the bulk rock in other cases (4417-1 and 4600-1),  
365 which is explained by relative concentration of smectite with respect to chlorite in the  $<0.2$   
366  $\mu\text{m}$  fraction.

367

### 368 ***FTIR data***

369

### 370 ***Identification of clay fractions***

371 The mid-infrared (MIR) spectra of the  $<0.2 \mu\text{m}$  fractions of XRD-identified end-member  
372 components (dioctahedral smectite from paleosol 4517-1, trioctahedral smectite from 4600-1,

373 and chlorite from Kob-23) were measured to serve as references (Figure 5). Spectra appear  
374 similar in the  $\nu\text{OH}$  region, exhibiting two broad bands centered at  $3624\text{ cm}^{-1}$  due to smectite  
375 or chlorite structural OH, and at  $3434\text{ cm}^{-1}$ , mainly due to water. For chlorite, the band at  
376  $3624\text{ cm}^{-1}$  is characteristically broader than for the other samples and is typical of  
377 trioctahedral chlorite (clinochlore type). For the dioctahedral smectite, the  $3624\text{ cm}^{-1}$  is  
378 characteristically narrower than for the other samples and is typical of montmorillonite (e.g.  
379 Madejová et al., 2017). For the trioctahedral smectite (4600-1), a shoulder at about  $3670\text{ cm}^{-1}$   
380 is observed in addition to the  $3624\text{ cm}^{-1}$  band. Such bands are found in griffithite (Madejová  
381 et al., 2017), which was previously identified as a trioctahedral iron-rich saponite (Komadel et  
382 al., 2000). Note that for saponite depleted in iron, the  $\nu\text{OH}$  is narrow and centered at  $3678\text{ cm}^{-1}$ .  
383 The spectra of the two other samples Mokrany-3B and 4504-1A are similar to 4600-1.

384 The  $1200\text{-}400\text{ cm}^{-1}$  region was more discriminant for sample characterization. The  
385 dioctahedral smectite could be unambiguously identified as montmorillonite through the  
386 occurrence of  $\delta\text{Al}_2\text{OH}$  and  $\delta\text{AlMgOH}$  specific vibration bands at  $920$  and  $837\text{ cm}^{-1}$ ,  
387 respectively (e.g. Madejová et al., 2017). A shoulder at  $878\text{ cm}^{-1}$  due to  $\delta\text{AlFe}^{3+}\text{OH}$  indicated  
388 that the montmorillonite contains some octahedral trivalent iron. The spectra of the 4600-1  
389 and 4504-1A samples corresponded clearly to griffithite with the characteristic bands at  $1016$ ,  
390  $678$  and  $452\text{ cm}^{-1}$  and shoulders at  $740$  and  $520\text{ cm}^{-1}$  (Madejová et al., 2017). The two strong  
391 bands at  $1016$  and  $452\text{ cm}^{-1}$  are respectively due to  $\delta\text{Si-O}$  and  $\delta\text{Si-O}$ , whereas the  $678\text{ cm}^{-1}$   
392 band is mainly due to  $\delta(\text{Fe}^{2+},\text{Mg})_3\text{OH}$  and indicates clearly the trioctahedral nature of the  
393 smectite. The Mokrany-3B spectrum revealed quartz in mixture with griffithite. The small  
394 shoulders at  $876$  and  $912\text{ cm}^{-1}$  indicated the occurrence of octahedral aluminium and trivalent  
395 iron in dioctahedral configuration.

396

397 **Comparison between clay component in chlorophaeite and the surrounding basalt**

398 As seen in Figure 6, the clay components in chlorophaeite are the same as those in the  
399 surrounding basalt. Indeed, for Mokransy-3A and Mokransy-4A, the spectra revealed the same  
400 features as for Mokransy-3B described above. The clay component is then griffithite (see  
401 above). The slightly more pronounced dioctahedral features (shoulders at 878 and 912  $\text{cm}^{-1}$   
402 due to of  $\delta\text{Al}_2\text{OH}$  and  $\delta\text{AlFe}^{3+}\text{OH}$ ) in Mokransy-4A indicated a higher content of octahedral  
403 aluminium and trivalent iron in dioctahedral configuration than in Mokransy-3A. For  
404 Mokransy-1A, the difference between the two spectra was the occurrence of feldspars in the  
405 surrounding basalt that hide the clay component features. However, in both samples griffithite  
406 could be identified and no dioctahedral features could be observed. The variability of  
407 chlorophaeite composition detected in MIR was also well expressed in NIR (near infrared),  
408 where the clay features could be observed without overlapping by quartz or feldspars.

409

#### 410 ***Organic geochemistry data***

411

412 All the rock samples investigated in this study contain organic matter (OM), but total organic  
413 carbon (TOC) content did not exceed 0.2%. The main constituents of OM in silylated total  
414 extracts (Figure 7A) were *n*-alkanes and fatty acids (FAs). The distribution of these  
415 biomarkers in the basalt sample 4600-3B differs significantly from other samples (Figure 7B):  
416 long-chain *n*-alkanes and *n*-alkanoic acids with the maxima between  $\text{C}_{23}$  and  $\text{C}_{29}$ , and  $\text{C}_{22}$  and  
417  $\text{C}_{30}$  carbon atoms, respectively, are present in relatively high concentrations. The values of  
418 short-chain to long-chain ratio (SCh/LCh) for *n*-alkanes and FAs for 4600-3B are 2.64 and  
419 1.27, respectively, whereas they are 9.12 and 29.81 for 4600-3A. Moreover, OM in sample  
420 4600-3B is characterized by the predominance of high molecular weight odd-carbon-  
421 numbered *n*-alkanes and even-carbon-numbered FAs, with the carbon preference index (CPI)  
422 values of 1.70 ( $\text{CPI}_{(25-31)}$ ) and 1.30 ( $\text{CPI}_{\text{total}}$ ) for *n*-alkanes, and 7.43 ( $\text{CPI}_{\text{f.a.}(20-30)}$ ) for FAs (for

423 CPI formulas see Rybicki et al., 2016). In the clay sample 4600-3A such predominance is not  
424 evident ( $CPI_{(25-31)}=1.01$  and  $CPI_{total}=0.83$ ).

425

#### 426 *Alteration petrography of chlorophaeite-bearing flood basalts*

427

428 The primary components of basaltic rocks identified by the petrographic observations are  
429 pyroxenes (ortho- and clinopyroxene), Ca-Na plagioclases, Fe,Ti oxides (titanomagnetite and  
430 ilmenite) and a homogeneous orange-brown isotropic substance presenting all the  
431 characteristics of chlorophaeite, as identified in several basaltic fields (Peacock and Fuller,  
432 1928). Such isotropic material occurs in several petrographic settings: (1) areas of intersertal  
433 mesostasis through the body of the basaltic rocks (Figure 8A), (2) filling or lining of circular  
434 cavities (Figure 8B), (3) veinlets and associated infilling of dicitaxitic voids in the basaltic  
435 rock (Figure 8C), (4) pseudomorphs after orthopyroxene (Figure 8D).

436 In the least altered basalts (sample 4522-1), chlorophaeite is totally isotropic at a  
437 microscopic scale and it contains fine networks of minute cracks, which tend to be more  
438 developed when observed under vacuum (evidence of water content). In the cavities,  
439 chlorophaeite occurs as irregular films showing frequently collomorphous texture typical of  
440 precipitation of a gel material (Figure 8B).

441 Chemical microanalysis of the isotropic material observed in thin sections confirms its  
442 chemical homogeneity (Table 2). The sum of oxide weight percent, which does not exceed  
443 85%, indicates a high water content of this isotropic material. Silicon and iron ( oxidation  
444 state not determined from EDS) are dominant, with subordinate Mg, Al and Ca, and minor  
445 amounts of alkali elements (Na, K). Such a composition reasonably agrees with the formula  
446 given by Peacock and Fuller (1928) for chlorophaeite:  $(Fe,Al)_2O_3 \cdot 2(Mg,Fe,Ca)O \cdot 4SiO_2 +$   
447  $10H_2O$ .

448 Observation of secondary mineral infillings indicates that chlorophaeite was deposited  
449 after the crystallization of quartz on the walls of vesicles and before the crystallization of  
450 chlorite, which cements the central parts of the vesicles. In the absence of phyllosilicates,  
451 minerals of the zeolite group are commonly observed as the late mineral cement of the  
452 residual open spaces of the basaltic rocks.

453 Smectitic clays were observed systematically as alteration products of the  
454 chlorophaeite bearing basaltic rocks. In the less altered basalts (sample 4522-1), the  
455 occurrences of smectitic clays are limited to minute spherules replacing chlorophaeite close to  
456 the contacts with the primary minerals of basalt (Figure 8E). Detailed observations with SEM  
457 indicate that such spherules are alteration features of chlorophaeite with a typical concentric  
458 structure. Smectitic clays, rimmed by a thin iron rich layer, were observed in the inner part of  
459 the spherule. The transition to unaltered chlorophaeite is marked by an external alteration  
460 halo, due to increasing microporosity and/or hydration of the initial isotropic material (Figure  
461 8F).

462 Chemical microanalysis of smectitic clays formed in the spherules indicates a close  
463 chemical similarity with that of the chlorophaeite starting material, except for lower iron and  
464 higher Mg and Al in the smectite (Table 2). The thin iron rich layer of the spherules likely  
465 accommodates the excess iron released during the alteration process of chlorophaeite.

466 In moderately altered samples (sample 4519-0), most of chlorophaeite lost its isotropic  
467 optical characteristics because of replacement by spherulitic and ribbon-like smectitic clays.  
468 Furthermore, primary or the previously formed hydrothermal minerals present features of  
469 partial dissolution. This is particularly the case for the iron rich phyllosilicates such as Fe-  
470 chlorite (Figure 8G). It should be noted that quartz presents also some evidence of dissolution  
471 at the contact with the smectitic clays (Figure 8H). In strongly argillized samples (4603-1, and

472 4603-4), chlorophaeite is totally replaced by smectitic clays and the basaltic primary minerals  
473 are partially replaced by smectitic clays and minerals of the zeolite group.

474

475 ***O and Fe isotope data***

476

477 Oxygen isotope data were collected for a range of bulk basalts showing variable alteration  
478 intensity, for a few clay vein and tuff samples, and for selected clay fractions <0.2  $\mu\text{m}$  (Table  
479 1). The least altered basaltic rocks have oxygen isotope values of 5.6 to 8.4 ‰. Basalts with  
480 increasing amount of alteration as well as tuffs have elevated  $\delta^{18}\text{O}$  values ranging from 10.1  
481 to 20.0 ‰, similar to the isotope range of clay separates (17.8 to 21.0 ‰), and green clays  
482 from veins and cavities (10.1 to 17.0 ‰). The paleosol samples have elevated oxygen isotope  
483 values of 21.3 to 21.7 ‰ and the chlorophaeite sample has the highest measured value of 23.0  
484 ‰.

485 A few of these <0.2  $\mu\text{m}$  clay fractions were also analyzed for iron isotope  
486 compositions (Table 1). In moderately altered basalts, the measured  $\delta^{56}\text{Fe}$  values are positive  
487 (0.028 for Mokranj-3B), but become negative with increasing alteration (down to -0.574 for  
488 Kob-23).

489

490 ***K-Ar dating of aluminoceladonite and illite-smectite***

491

492 Selected 2-0.2 and <0.2  $\mu\text{m}$  fractions of tuffs containing aluminoceladonite and illite-smectite  
493 were dated, at least twice, in order to establish the age of potassic alteration (Table 3). The  
494  $\text{K}_2\text{O}$  contents vary from 1.785 % for the sample Tashki-10, with minor amounts of  
495 aluminoceladonite and illite-smectite, to 6.71% for Kob-9B, dominated by aluminoceladonite

496 (comp. Inline Supplementary Figure 4). The measured ages range from  $447.5 \pm 2.5$  to  $296.0 \pm 5$   
497 Ma.

498

## 499 **Interpretation**

500

### 501 *Alteration of flood basalts*

502

#### 503 *Mineral changes*

504 No single sample was identified by XRD to be composed exclusively of primary basalt  
505 minerals: Ca-plagioclase, pyroxene, magnetite, ilmenite, and pseudobrookite. All samples  
506 contain hydrated components (mostly clays), but in variable quantities. If the sum of primary  
507 basalt minerals is accepted as an inverse index of basalt alteration, and if the degree of  
508 alteration is interpreted as a chronosequence (stronger alteration considered as a subsequent  
509 step of the process), a clear pattern of basalt alteration emerges, which can be described by  
510 five steps (Inline Supplementary Table 1), leading from almost fresh basalt to completely  
511 altered rock, though still preserving the basalt texture.

512 In the investigated samples, the earliest alteration products are quartz with  
513 trioctahedral smectite, or with a mixture of di- and trioctahedral smectite, all together < 10  
514 wt%. This is also the mineral composition identified in chlorophaeite accumulations, found in  
515 basalts with more advanced alteration (compare Mokraný samples in Inline Supplementary  
516 Table 1). Based on this identity and on the microscope observations, we assume that the early  
517 quartz did not crystallize from melt but it is a product of basalt alteration (mostly of volcanic  
518 glass), deposited in crystal interstices or in larger chlorophaeite accumulations. Thus, step I  
519 can be identified tentatively as predominantly the alteration of volcanic glass. Emetz et al.  
520 (2006) also identified quartz as an alteration mineral based on petrographic observations.

521 In step II (90-80 % primary minerals), orthoclase/sanidine and hematite appear and  
522 the amount of smectites increases compared to step I. In step III (80-60 % primary minerals),  
523 chlorite appears, hematite, quartz and smectite abundances increase, pyroxene decreases, and  
524 ilmenite is absent. In step IV (60-25% primary minerals), anatase, analcime, zeolites and  
525 calcite appear, smectite, quartz and orthoclase/sanidine increase further, plagioclase starts  
526 decreasing, and pyroxene and pseudobrookite disappear. In step V (<25% primary minerals),  
527 plagioclase and magnetite disappear, and dioctahedral smectite plus chlorite prevail over  
528 trioctahedral smectite. The mineral composition of green clay veins and cavities in basalts is  
529 similar to the most altered basalts of step V. Ubiquitous hematite indicates an oxidizing  
530 alteration environment. In general, the lower basalts appear more altered than the upper  
531 basalts. Petrographic study confirmed the crystallization of smectite both before and after  
532 chlorite.

533

#### 534 *Chemical changes*

535 The mineral alteration of basalt is paralleled by characteristic chemical changes, which are  
536 surprisingly limited (Inline Supplementary Table 4) considering the extent of alteration  
537 observed in some samples. The most pronounced is the decrease of CaO from 10% almost to  
538 0% (except of samples with abundant calcite). The progressing dissolution of Ca-plagioclase  
539 results in the removal of Ca from the system (Inline Supplementary Figure 6). Sr decreases  
540 along with Ca. In steps IV and V, when plagioclase decreases strongly and analcime and other  
541 zeolites appear, Na seems to undergo redistribution: it is depleted from rocks without zeolites  
542 and enriched in remaining rocks.

543 The most pronounced gain during basalt alteration is the sum of OH and H<sub>2</sub>O in clays,  
544 represented by the loss on ignition (LOI), which increases from almost 0% to 6.5% in samples  
545 free of calcite. The correlation of sum of clay with LOI is very high and extrapolates to 0 for

546 unaltered basalt and to 9% for completely altered basalt. The trend line runs between values  
547 characterizing smectitic and chloritic green clay veins in basalt (Figure 9), in agreement with  
548 the intermediate, smectite+chlorite composition of clays in strongly altered basalt. LOI can  
549 serve as a simple measure of the degree of basalt alteration.

550 In the course of alteration, basalts also gain MgO, which increases about two times:  
551 from 5 to 10% and is positively correlated with the sum of clays (Figure 9), except of the  
552 samples with carbonates (not shown in the figure). Boron increases even more, in particular in  
553 steps IV and V, and good positive correlation indicates that B is located in the dioctahedral  
554 clay (Inline Supplementary Figure 7). Some increase in K, Cs, and Rb is also observed, and  
555 these trends can be best explained by combined contributions from K-spar and dioctahedral  
556 clay (Inline Supplementary Figure 8), which is partially illitized during much younger  
557 Paleozoic events (see below), particularly in highly altered basalts (Inline Supplementary  
558 Table 3).

559 The remaining elements vary, but no trends related to the degree of alteration can be  
560 observed (Inline Supplementary Table 4). The mass of basalt during alteration essentially  
561 does not change, because the additions and subtractions of elements quantitatively  
562 compensate. This mass stability is best expressed by very stable SiO<sub>2</sub> and Al<sub>2</sub>O<sub>3</sub> contents. The  
563 collected data do not indicate measurable chemical changes between the lower and upper  
564 flood basalts.

565 REE patterns of most basalt samples are very similar and characteristic of the  
566 continental flood basalts (Farmer, 2003): enriched in LREE and without an Eu anomaly  
567 (Figure 10). REE do not differentiate the lower from the upper basalts. LREE seem slightly  
568 depleted at the final alteration step, particularly in the rock with high chlorite content (Kob-  
569 22), but otherwise basalt alteration does not affect the REE pattern, despite sometimes total  
570 destruction of major primary minerals. Inline Supplementary Figure 9 indicates that LREE in

571 basalts seem mostly contained in phosphates, of too low content to be detectable  
572 mineralogically (Inline Supplementary Table 1).

573 In chlorophaeite, LREE are strongly concentrated, compared to regular basalts, while  
574 HREE are depleted, and a strong negative Eu anomaly is present (Mokrany-3A in Figure 10  
575 and Inline Supplementary Figure 9). This composition confirms the origin of chlorophaeite  
576 from the volcanic glass, enriched in incompatible LREE, while depleted in Eu contained in  
577 plagioclase (Weill and Drake, 1973) and depleted in HREE, which form isomorphic  
578 substitutions in pyroxene (Rollinson, 1994; Kuzmenkova, 2009). The basalt sample hosting  
579 chlorophaeite concentrations (Mokrany 3B in Figure 10 and Inline Supplementary Figure 9)  
580 displays analogous characteristics. Both have much higher LREE/P<sub>2</sub>O<sub>5</sub> ratio compared to  
581 regular basalts (Inline Supplementary Figure 9). These characteristics are similar to  
582 rhyodacite samples, which also differ from basalts by elevated LREE, negative Eu anomaly  
583 (Figure 10), and much higher LREE/P<sub>2</sub>O<sub>5</sub> ratio (Inline Supplementary Figure 9).

584

#### 585 *Oxygen isotopes and Fe<sup>2+</sup>/Fe<sup>3+</sup> ratio*

586 The progress of basalt alteration can be traced also by oxygen isotope compositions of the  
587 bulk rock samples (Table 1, Figure 11). They evolve linearly and extrapolate to a value close  
588 to 5‰ for the unaltered protolith, consistent with the oxygen isotope composition of unaltered  
589 continental flood basalts that show little to no contamination by continental crustal material  
590 (e.g. Harmon and Hoefs, 1995; Eiler 2001), and to the value of about 22‰ for complete  
591 alteration, similar to the isotopic compositions of smectite from the weathering zone (4529-2  
592 and 4517-1) developed on basalts. A similar value of 23‰ characterizes the measured  
593 chlorophaeite sample, composed exclusively of secondary minerals (Mokrany-3A) and the  
594 clay fraction separated from the host basalt (Mokrany-3B<0.2). In Figure 12, the equilibrium  
595 relationships between oxygen isotope composition of smectite, of water, and temperature,

596 based on the fractionation equation of Sheppard and Gilg (1996) are depicted. The smectite-  
597 rich paleosol samples are in equilibrium with waters of about -5 ‰ at ambient temperatures.  
598 Using this isotope value of meteoric water, temperatures of dioctahedral smectite alteration in  
599 the basalts is estimated at less than 40°C. On the other extreme, if only magmatic water with a  
600 heavy oxygen isotope composition of +5‰ is assumed as the clay-forming fluid, then  
601 temperatures of about 100 to 130°C are indicated for the dioctahedral smectite formation.

602 Another parameter correlating well with the applied index of basalt alteration is %  
603 Fe<sup>2+</sup> of the bulk rock measured by Mössbauer spectroscopy (Table 1, Figure 13). The only  
604 measured chlorophaeite sample also fits this trend (Mokraný-3A). The linear trend  
605 extrapolates to ca. 67% for pure basalts and falls to 30% at ca. 40% of primary minerals,  
606 where those containing Fe almost disappear. Fe<sup>2+</sup> was lost due to oxidation, and not removal  
607 under anoxic conditions, as Fe content of the rock remained stable (Inline Supplementary  
608 Table 4). This trend implies that basalt alteration from the very beginning involved water  
609 carrying oxygen, in agreement with the increasing content of hematite.

610 The most altered samples (Kob-15 and 4417-1) and green clays from veins and  
611 cavities (4600-1 and Kob-23) fall off the general trend, as their % Fe<sup>2+</sup> is much higher (Table  
612 1, Figure 13). This implies higher % Fe<sup>2+</sup> of clays at this stage of alteration, which agrees well  
613 with the Mössbauer estimates of % Fe<sup>2+</sup> in clay fractions of rocks (Figure 13), the Mössbauer  
614 data for tuffs, and the abundance of chlorite in these rocks. These data lead to the conclusion  
615 that at the most advanced stage of alteration, the conditions became more reducing.

616

### 617 *Alteration of organic compounds*

618 The primary distribution of particular organic compounds depends on the source of OM and  
619 can be modified by a wide range of post-depositional processes. Algae and bacteria generate  
620 short-chain *n*-alkanes with preponderance of C<sub>17</sub> and C<sub>19</sub> carbon atoms in the molecule, while

621 terrestrial higher plants (especially their leaf epicuticular waxes) are characterized by the  
622 occurrence of long-chain *n*-alkanes and *n*-fatty acids (*n*-FAs). Our studies evidenced a clear  
623 predominance of long-chain *n*-alkanes and *n*-FAs (excluding C<sub>16</sub> and C<sub>18</sub>) with majority of an  
624 odd and even number carbon atoms in the molecules, respectively, in most of the Ediacaran  
625 sedimentary rocks from the EEC (Goryl and Marynowski, 2016). Bobrovskiy et al. (2018)  
626 suggested that a possible source of long-chain *n*-alkanes in the Ediacaran rocks are spherical  
627 cyanobacterial colonies. The level of thermal maturity of the Ediacaran OM from the EEC is  
628 unusually low (the estimated equivalent of vitrinite reflectance did not exceed 0.57% R<sub>r</sub>)  
629 which promoted preservation of the primary character of distribution of organic compounds  
630 (Pehr et al., 2018; Goryl et al., 2018).

631 We believe that OM from the basalt sample 4600-3B is the most primary, non-  
632 oxidized or only slightly oxidized remnant of the Ediacaran cyanobacteria (and other  
633 microorganisms?) activity in the basalt hydrothermal system. Decay of long-chain *n*-alkanes  
634 and *n*-FAs and decreasing value of CPI in all other samples indicate more intense oxidation of  
635 OM in paleosols and in clays from cavities. Similar effect of OM alteration was presented by  
636 Elie et al. (2000, 2004): gradual degradation of long-chain *n*-alkanes and *n*-alkanoic acids  
637 during artificial oxidation of argillaceous rocks. Also Marynowski and Wyszomirski (2008)  
638 presented significant influence of early diagenetic oxidation on *n*-alkanes and other organic  
639 compounds distribution on an example of green and red Triassic clays. It seems that in the  
640 basaltic rock, primary OM was better protected against oxidation by the Ediacaran  
641 hydrothermal processes and further Caledonian and/or Variscan alterations. Such  
642 cyanobacteria activity offers a feasible explanation of more reducing conditions observed at  
643 the final stages of basalt alteration.

644

#### **Characteristics of the basaltic smectite**

For three available pure smectitic samples (<0.2  $\mu\text{m}$  fractions) with variable ratios of di- and trioctahedral components, the chemical data (Inline Supplementary Table 4), including  $\text{Fe}^{2+}/\text{Fe}^{3+}$  ratio from the Mössbauer spectroscopy (Table 1), were cast into structural formulae (Table 4). The amount of potassium is very low, consistent with the XRD characteristics (Inline Supplementary Table 3, Inline Supplementary Figure 2).

645           The chemical compositions of the three smectitic samples evolve in a regular manner,  
646 consistent with the XRD evaluation of di/tri-smectite ratio (Table 4). The calculated numbers  
647 of octahedral cations are between 2 and 3 per half unit cell and they can be used as a measure  
648 of di/tri-smectite ratio. Plots of other data with respect to these numbers are linear ( $R^2 = 0.92-$   
649  $0.99$ ) and allow extrapolating compositions of the end member components (Table 5). The  
650 dioctahedral smectite end member is a perfect montmorillonite without tetrahedral  
651 substitution, high Fe and Mg contents, and no divalent iron, as confirmed by Mössbauer  
652 spectra of the dioctahedral smectite component (Table 1) and dioctahedral smectite identified  
653 from basalt weathering zones by Liivamägi et al. (2018). Its oxygen isotope characteristics  
654 and its positive  $d^{56}\text{Fe}$  are also similar to the montmorillonites from paleosols, which are  
655 however much more rich in Al (op. cit.). The dioctahedral smectite has been partially illitized  
656 during the Paleozoic thermal events (see below).

657           Almost all REE is contained in the dioctahedral clay, which is consistent with their  
658 trivalent character (the dioctahedral sheet accepts mostly trivalent cations). Exceptionally low  
659 REE content of chlorite Kob-23 (Figure 10), which contains 95% of divalent iron (Table 1) is  
660 consistent with this interpretation of REE segregation. Thus dioctahedral clays are partially  
661 responsible, along with phosphates, for the REE budget of the investigated rocks. This  
662 conclusion is confirmed by  $\text{P}_2\text{O}_5$  depletion in clay fractions compared to the bulk rock (Inline  
663 Supplementary Table 4), parallel to the LREE enrichment in the clay fraction with dominant  
664 dioctahedral component (Mokraný-3B). REE seem to be incorporated in the dioctahedral clay

665 structure and not adsorbed like in weathering clays (Bau, 1991), as the clay fractions were  
666 analyzed after Na-exchange. The location of REE in clay structure indicates that they became  
667 available at the time of clay crystallization and not later. Otherwise they would occupy the  
668 exchange sites.

669 The trioctahedral smectite end member is almost ideal iron-rich saponite, with 0.84  
670 Al<sup>IV</sup>, no Al<sup>VI</sup>, very high Mg, and Fe not much higher than in the dioctahedral clay, but ferrous  
671 in 42%. Its  $\delta^{18}\text{O}$  value is much lower than in di-smectite and its  $\delta^{56}\text{Fe}$  is negative, like in  
672 chloritic trioctahedral clays (Table 1).

673 XRD, chemistry and FTIR data are consistent and detect variable di/tri ratio of the  
674 investigated basaltic smectites. Based on the XRD evidence (separate 02 and 06 reflections)  
675 and very different REE contents and oxygen and iron isotope ratios, the smectitic clay  
676 component of Volyn basalts is interpreted here not as a mineral but as a mixture of iron-rich  
677 montmorillonite and iron-rich saponite. This mineral mixture occurs both in basalts and in the  
678 chlorophaeite accumulations (Figure 3 and Inline Supplementary Figure 3). A similar material  
679 was identified by Faust (1955), Ross (1960), and Komadel et al. (2000) as iron di-  
680 trioctahedral saponite, and named griffithite. Formulae of griffithite calculated from Ross  
681 (1960) and Komadel et al. (2000) data (Table 4) and the XRD data, obtained for Komadel et  
682 al. (2000) sample (Inline Supplementary Figure 3), suggest that it is also a mineral mixture,  
683 close to our sample 4600-1. The reported griffithite formulae differ strongly in the degree of  
684 iron oxidation, which may reflect sample heterogeneity and/or the measurement technique.  
685 Both samples come from the same original griffithite locality at Griffith Park in California,  
686 but may represent slightly different material. Other samples from this area are end-member  
687 Fe-saponites with high Fe<sup>3+</sup>/Fe<sup>2+</sup> ratios (Treiman et al., 2014).

688 Very similar materials, named oxysmectites, were described by Dainyak et al. (1981)  
689 and Simanovich et al. (2010) from continental flood basalts of Siberia (Table 4) and from an

690 oceanic basalt sample. The continental sample has di/tri ratio close to our 4504-1 but it has  
691 more Fe than Mg. A pure trioctahedral analogue of our sample 4600-1, but with Fe dominant  
692 over Mg (Table 4), was identified in a Siberian hydrothermal deposit and called ferrosaponite  
693 (Chukanov et al., 2004), the name accepted by IMA (Jambor and Roberts, 2004). Numerous  
694 occurrences of similar materials were reviewed by Sarkar et al. (2016), who identified  
695 ferrosaponite in continental basalts.

696 The relative enrichment of montmorillonite in the heavy Fe isotope compared to Fe-  
697 saponite is consistent with the general rule that the oxidized form of Fe is enriched in heavy  
698 isotopes (Teutsch et al., 2009 and literature cited). Negative  $\delta^{56}\text{Fe}$  values of chloritic samples  
699 (Table 1), which contain only  $\text{Fe}^{2+}$ , support this interpretation. Comparable or even higher  
700 fractionations of iron have been observed during oceanic basalt alteration and interpreted as  
701 abiotic (Rouxel et al., 2003), though a biotic involvement cannot be excluded in our case, as  
702 the dissimilatory iron reduction is regarded as the most efficient mechanism for generating  
703 isotopically light  $\text{Fe}^{2+}$  (Wu et al., 2010), and the presence of unaltered organic matter in basalt  
704 has been documented in previous sections.

705 Major differences in  $\delta^{18}\text{O}$  values between di- and trioctahedral smectite could be  
706 related to formation from the same fluid at different temperatures with trioctahedral smectite  
707 forming at ca. 50°C higher temperatures if fractionation factors are similar (Figure 12).  
708 However, theoretical considerations (Savin and Lee, 1988; Kohn and Valley, 1998) and  
709 empirical data (Craw et al., 1995) suggest that oxygen isotope fractionation between smectite  
710 and water is about 5 ‰ smaller for Mg-rich smectite than for Al-rich smectite. Thus, di- and  
711 trioctahedral smectites may have formed at similar temperatures and from the same fluid. On  
712 the other hand, the temperature difference may have been higher, if trioctahedral smectites  
713 formed from a fluid with magmatic component (isotopically heavier).

714 Petrographic observations document the appearance of early smectite as the alteration  
715 product of isotropic material, which was described earlier in many publications under the  
716 name “chlorophaeite”. It was deposited during hydrothermal processes, cementing  
717 successively the residual open spaces of the basaltic rocks. Under the microscope  
718 chlorophaeite appears isotropic only in the least altered rocks, and during progressing  
719 alteration it gradually evolves into birefringent smectite. This alteration is almost isochemical,  
720 but some iron is lost (Table 2). In XRD, smectite from the chlorophaeite accumulation in least  
721 altered basalt differs from others by more trioctahedral character and much smaller crystal  
722 thickness, evidenced by more diffuse 001 reflection (Figure 3). NIR spectra indicate that it is  
723 richer in Fe, without detectable Al contribution. Combining these observations, we suggest  
724 that the isotropic substance is a trioctahedral smectite close to ferrosaponite, with extremely  
725 fine crystal size, which results in the isotropic characteristics. It may have been deposited  
726 originally as an amorphous material, but no clear evidence of such material was found in the  
727 investigated samples. Smectite crystallizing from an amorphous material is known to form  
728 originally extremely thin, even monolayer crystals (Derkowski et al., 2015 and references  
729 therein). In the course of further alteration, ferrosaponite alters into a mixture of Fe-  
730 montmorillonite and Fe-saponite with well-developed multi-layer crystallites. At early stages,  
731 the quantities of both smectites grow in parallel in the course of progressing alteration, but  
732 trioctahedral smectites grow at twice higher rate (Inline Supplementary Figure 10). Latter, the  
733 content of dioctahedral smectites continue to grow steadily, while the content of trioctahedral  
734 smectites levels off and starts decreasing, when the hematite content starts increasing. We  
735 interpret these relationships as indicative of the redox control over the process: as long as the  
736 conditions are relatively reducing, crystallization of trioctahedral smectite is favored, both by  
737 abundant  $Mg^{2+}$  and  $Fe^{2+}$ : the major constituents of the trioctahedral sheet. When  $Fe^{3+}$  becomes  
738 dominant, the crystallization of dioctahedral smectite is favored (trivalent ions dominant in

739 the dioctahedral sheet), and the decrease of trioctahedral smectite indicates that it is altered  
740 into chlorite and/or dioctahedral smectite at these advanced stages of basalt alteration.

741

#### 742 *Alteration of tuffs*

743

#### 744 Mineral changes

745 Mineralogically, tuffs (volcano-clastic rocks) differ strongly from flood basalts by their much  
746 broader range of quartz content, which, if elevated above basalt values, is always higher than  
747 K-feldspar content. The opposite relation, characteristic of flood basalts, is common in low  
748 quartz tuffs. If % quartz is plotted against % Kspar for all tuff samples (Inline Supplementary  
749 Figure 11) it becomes clear that the tuffs have a broad range of intermediate compositions,  
750 extending from basalts to the felsic rocks. Quartz content was used then as a proxy for this  
751 primary tuff mineral variability (Inline Supplementary Table 2), and tuffs were divided into  
752 samples close to basaltic composition (quartz <14%) and more felsic samples. In general,  
753 tuffs with >20% quartz are competent rocks and with lower content of quartz are friable.

754 The basaltic tuffs resemble by mineral composition the most altered flood basalts:  
755 some plagioclase still present in some samples, pyroxene and other primary minerals are  
756 absent, anatase is present, hematite, di- and trioctahedral smectite plus chlorite are abundant,  
757 and analcime is occasionally present. The apparent differences are the presence of albite and  
758 aluminoceladonite.

759 The felsic tuffs seem less altered because their calcic plagioclase content is much  
760 higher. They contain less anatase, hematite, trioctahedral smectite and chlorite. Only  
761 dioctahedral clay is as abundant as in basaltic tuffs, but more illitized. They also contain  
762 aluminoceladonite, but no albite or analcime. Kaolinite detected in the top samples of two

763 Kobryn tuffs are indicative of subaerial weathering and soil development before deposition of  
764 subsequent lava flows.

765

766 *Chemical changes*

767 The arrangement of tuff samples by % quartz reveals very clear trends in their chemical  
768 composition (Inline Supplementary Table 4). Towards the basaltic end, Si and K contents  
769 decrease to a level typical of basalt, while Fe, Al, Mn, Mg, Ti and LOI increase. Mg and LOI  
770 increase to the level characteristic for the most altered basalts, which is consistent with the  
771 mineralogical evidence. Among trace elements REE, Be, Ba, Cs, Nb, Rb, Sr, Ta, Th, U, Y,  
772 and Zr decrease, while Co, Cr, Cu, Ni, Sc, V and Zn increase. No measurable control of the  
773 trap stratigraphy (lower vs. upper basalts) over chemistry can be observed.

774 In accordance with these trends, average contents of most elements for tuffs are  
775 intermediate between values for flood basalts and rhyodacites, indicating that, like flood  
776 basalts, also tuffs were altered without a major change of mass. For a few elements, the  
777 averages for tuffs are higher than the end member values: B, Mg, LOI, Cr, Cs, Cu, Ni, and Pb.  
778 Such elevated values imply the import of these elements during alteration, similar to the  
779 detected in basalts (B, Mg, LOI, Cs) but including metals. Also in basalts metals are mobile,  
780 as recorded by the metals enrichment in chlorophaeite and clay fractions, as compared to their  
781 bulk basalt samples (Inline Supplementary Table 4). This conclusion is consistent with the  
782 observation of native copper and silver occurrences in association with chlorophaeite  
783 (Kuzmenkova et al., 2006a).

784 Elements commonly most immobile in rocks: Hf, Nb, Pr, and Zr, used as the mass  
785 balance references in weathering studies (e.g. Liivamägi et al., 2018) are much less abundant  
786 in basalts than in felsic rocks. They differentiate the studied rocks similarly to quartz content  
787 (compare Inline Supplementary Figure 11 and 12), confirming the classification of tuffs based

788 on mineralogy into more basaltic and more felsic. In general, also this approach does not  
789 differentiate lower from upper volcanics. Locally, subsequent levels of flood basalts and tuffs  
790 can be differentiated, as illustrated in Inline Supplementary Figure 13 for Kobryn profile,  
791 where three levels of tuffs and two levels of flood basalts have been sampled over ca. 150 m  
792 of depth. The tuff composition is clearly more felsic. On the other hand, four tuff samples  
793 from Tashki plot in Inline Supplementary Figure 9 outside the basalt field, indicating an even  
794 more basic composition than the available basalt samples. They represent bottom part of the  
795 volcanic sequence, where picrites and microbasalts were identified (Kuzmenkova et al., 2011;  
796 Shumlyanskyy et al., 2016).

797         The tuffs vary in color in most profiles, alternating from green to brown and even red.  
798 Green color is more common among more felsic tuffs. When compared with other tuffs of  
799 similar quartz content, green tuffs differ from brown tuffs only by less hematite and more U,  
800 which is consistent with more reducing local environment (evacuation of Fe, enrichment in U)  
801 but does not allow us to conclude whether this is a hydrothermal alteration feature or the  
802 result of a younger process. The lack of systematic difference in clay composition favors the  
803 latter explanation.

804

#### 805 **Oxygen isotopes and $Fe^{2+}/Fe^{3+}$ ratio**

806 Both sets of data collected for tuffs of basaltic composition do not follow trends characteristic  
807 of flood basalts and resemble data obtained for clay veins in basalts:  $d^{18}O$  values are lower (  
808 Figure 11) and %  $Fe^{2+}$  values are higher than extrapolations of basaltic trends to the zone of  
809 complete alteration (comp. Table 1 with Figure 13). These relations can be explained by  
810 higher abundance of chlorite in the analyzed tuff samples compared to the flood basalts  
811 (Supplementary Table 1 and 2), based on the %  $Fe^{2+}$  and the oxygen isotope data for Kob-23  
812 chlorite (Table 1).

813

814 **K-Ar dating of clay fractions**

815 Dates of replicate analyses and dates of two fractions all are within the error range for a given  
816 sample, thus they can be regarded as representing unique illitization episodes (Środoń et al.,  
817 2002). In the south (Tashki), the Carboniferous date of ca. 300 Ma was obtained, while in the  
818 north, dates range from 417 to 447 Ma. A very similar geographical distribution of ages was  
819 detected by dating aluminoceladonite and illite-smectite in paleosols developed on basalts  
820 (Liivamägi et al., 2018). Clearly, the potassic alteration episode affected tuffs and paleosols  
821 developed on flood basalts long after the formation of these rocks. Basalts were also affected,  
822 though to a lesser extent: aluminoceladonite was not formed, but smectite was slightly  
823 illitized (Supplementary Table 3).

824

825 **Discussion and conclusions**

826

827 Flood basalts and tuffs of the Volyn-Brest province were affected to a very different extent by  
828 two subsequent alteration episodes, the first pre-dating and the second post-dating the  
829 Ediacaran weathering of top surface.

830 The first alteration episode involved sequential destruction of volcanic glass and  
831 primary basaltic minerals and crystallization of secondary phases: tri- and dioctahedral  
832 smectite, chlorite and/or mixed-layer chlorite-smectite, hematite, quartz, anatase, and zeolites.  
833 Basalts which underwent Ediacaran weathering studied by Liivamägi et al. (2018) contained  
834 such secondary mineral assemblage.

835 The basaltic smectites are of unique composition: montmorillonite with high Fe<sup>3+</sup> and  
836 saponite also high in Fe, but with significant Fe<sup>2+</sup> content. Similar clays have been described

837 earlier from various basalt provinces under the names “chlorophaeite”, "griffithite" or  
838 "oxysmectite", and "ferrosaponite" if Fe>Mg.

839 The term “chlorophaeite” is used also in macroscopic descriptions to name  
840 accumulations of dark glassy matter in basalts. Such chlorophaeite accumulations do not  
841 contain primary basaltic minerals, but mainly secondary minerals characteristic of the first  
842 step of basalt alteration (quartz, tri- and dioctahedral smectite), also if chlorophaeite  
843 accumulations are contained in basalts of higher alteration step (Supplementary Table 1). In  
844 particular, they do not contain hematite, they are strongly enriched in Si and enriched in Mg  
845 and metals compared to the host basalt. These observations, along with the REE pattern,  
846 suggest that chlorophaeite accumulations are products of alteration of the amorphous material  
847 (solidified leftover melt, i.e. volcanic glass), in agreement with conclusions of many earlier  
848 researchers (Kuzmenkova et al., 2006b and the references cited), and that the alteration took  
849 place at the earliest stage, in non-oxidizing environment, but it is related to the same solutions  
850 that altered flood basalts and tuffs.

851 The subaerial location, the evolution of bulk rock  $Fe^{2+}/Fe^{3+}$  measured by Mössbauer  
852 spectroscopy, the evolution of bulk rock oxygen isotope composition, the presence of  
853 hematite, and the lack of depletion in Fe and Mn indicate that the basalt alteration involved  
854 oxygenated meteoric waters, probably heated and put in motion by the cooling basalt flows.  
855 Such heat-driven convection of meteoric water is a very effective mechanism of alteration of  
856 cooling volcanic bodies (e.g. Eberl et al., 1987). A similar mechanism of alteration of Volyn  
857 flood basalts was proposed by Melnychuk (2006), who envisioned the Ediacaran dolerite sills  
858 intruding basalts and the underlying sandstones as the source of heat. The heat-driven  
859 convection mechanism explains well the observed major enrichment in Mg, brought by  
860 upflow from deeper parts of the basalt body, where olivine and pyroxene are early subjects to  
861 alteration. The alteration sequence is analogous to these reported from other hydrothermal

862 subaerial, hydrothermal submarine, and burial metamorphic alterations of basalts, including  
863 the difference in Si/(Si+Al) and Fe/(Mg+Fe) ratios between the smectitic and chloritic clays  
864 (Table 4). The alteration conditions were more oxidizing, which is manifested by the presence  
865 of hematite from early stages of the alteration process. A rare feature for the basalt alteration  
866 series is the abundant development of dioctahedral smectite, which continued later during the  
867 weathering stage, as documented by Liivamägi et al. (2018). The alteration proceeded from  
868 outside into the basalt layers, as observed also earlier (Juskowiakowa, 1974), and in extreme  
869 cases it was complete: all basaltic minerals were altered but the basalt texture was preserved.  
870 Our data indicate that microbial organisms participated in the hydrothermal alteration process,  
871 which is consistent with earlier evidence of the microbial life on the Ediacaran land in this  
872 area (Kremer et al., 2018; Liivamägi et al., 2018).

873         Compared to flood basalts, the alteration of tuffs of basaltic composition is much more  
874 advanced, which seems related to their high porosity and permeability. Mineralogically, they  
875 differ by much more abundant chloritization, and albitization not noted in basalts. The  
876 alteration of rhyodacites and tuffs of felsic composition seems less advanced than basaltic  
877 tuffs but more advanced than of the neighboring flood basalts, as best illustrated by the  
878 Kobryn profile (Supplementary Table 2). The abundance of felsic tuffs in the entire profile of  
879 the volcanic province indicates that felsic volcanism was active during much longer period  
880 than indicated by the known felsic lavas of the middle volcanogenic series (e.g. Kuzmenkova  
881 et al., 2011).

882         The detected mineral assemblage: from smectite to chlorite with zeolites, but without  
883 major albitization, epidote, actinolite, or amphibole puts the upper temperature limit of post-  
884 magmatic, pre-weathering alteration at ca. 220°C and lower at 50°C, based on the calibration  
885 in the Icelandic active hydrothermal systems (Franzson et al., 2008: cf. Introduction) and  
886 many other smectite-to-chlorite transformation series reviewed by Robinson et al. (2002). The

887 evidence of such maximum temperature conditions comes from most tuffs and the most  
888 altered flood basalts. Low  $\delta^{18}\text{O}$  of chlorite (10.1‰ for Kob-23 sample) is consistent with a  
889 temperature of 190°C if a magmatic fluid with ca. 6‰ is assumed (Cole and Ripley, 1998). In  
890 this scenario, chlorite is considered as an indicator of a higher temperature overprint, which  
891 altered older iron saponite, formed by the interaction of basalt with the heated meteoric  
892 waters. Locally, the temperatures of Ediacaran alteration may have been even higher, as  
893 albite, prehnite, and pumpellyite were reported (Emetz et al., 2006; Melnychuk, 2006), and  
894 epidote was identified in the olivine pseudomorphs in samples from west Belarus (Skveriki  
895 well: Kuzmenkova, 2009.). On the other hand, most flood basalts were altered by much cooler  
896 fluids, as evidenced by the lack of chlorite and by the preservation of fresh organic material.  
897 Our data confirm earlier observations that the extent of basalt alteration is controlled by the  
898 temperature and permeability. Figure 14 presents a synthetic model of the basalt alteration  
899 during the hydrothermal episode.

900         The second alteration episode, evidenced by K-Ar dating (Table 1 and Liivamägi et  
901 al., 2018) and detected earlier by Ar-Ar of the whole rock samples (Elming et al., 2007),  
902 involved the crystallization of aluminoceladonite and potassium feldspar (Liivamägi et al.,  
903 2018) and alteration of dioctahedral smectite into illite-smectite. K-Ar identifies two thermal  
904 events on the cratonic foreland of neighboring orogenic systems: in more northern locations  
905 (Belarus and Poland) related to the Caledonian orogeny, and in Volyn – to the Variscan.

906         This late diagenetic alteration affected porous tuffs to a greater extent than flood  
907 basalts, and within the flood basalts, it preferentially affected samples more intensely altered  
908 by the first alteration episode, i.e. with higher secondary porosity. The temperature of this late  
909 alteration was not higher than 85°C, according to illite-smectite data from the overlying  
910 sediments (Liivamägi et al., 2018) or even lower, according to the organic geochemistry data

911 (Goryl et al., 2018). Apparently, in a high-Mg environment, aluminoceladonite can  
912 crystallize at relatively low temperatures.

913         Inline Supplementary Figure 7 demonstrates that potassium was imported into basalt  
914 during the diagenetic alteration. In addition to potassium, enrichments in Cs, Rb, and B in  
915 basalts can be also explained by this diagenetic event, based on their observed positive  
916 correlations with % K<sub>2</sub>O and % dioctahedral clay, and established knowledge of their  
917 behavior (cf. Derkowski and McCarty, 2017 for Rb and Cs, and Środoń, 2010 for B). For  
918 tuffs, such reasoning cannot be made, as their original K<sub>2</sub>O content is variable. Thus it  
919 remains unclear whether K<sub>2</sub>O, Cs, Rb, and B imported into flood basalts were derived locally  
920 from felsic tuffs, or if these elements result from a more long-range transport.

921         Hydrothermal alteration of the Volyn-Brest basalt trap, in continental settings and  
922 driven by heat of the cooling traps, can be considered as a good Earth analogue of the  
923 Noachian basalt alteration on Mars. The Noachian alteration also produced Fe-rich smectites  
924 and hematite (e.g. Ehlmann et al., 2011; Carter et al., 2103; Chemtob et al., 2015), which are  
925 also interpreted as a result of subsurface basalt interaction with heated ground waters  
926 (Ehlmann et al., 2011b), and are investigated with the techniques used in this study (XRD:  
927 e.g. Blake et al., 2012, Downs et al. (2015); Mössbauer: e.g. Klingelhöfer et al., 2004; NIR:  
928 e.g. Carter et al., 2013; Bishop et al., 2017). Particularly useful for Martian studies should be  
929 (1) detail characterization of the Fe-smectite alteration products, which are also dominant on  
930 Mars and in particular the role of redox in controlling the di/tri-smectite ratio; (2) detecting  
931 Mg enrichment during the alteration, considered indicative for the proposed alteration  
932 mechanism, and inconsistent with weathering models (e.g. Le Deit et al., 2012); (3) limited  
933 chemical changes despite radical changes in mineralogy, indicative for the proposed alteration  
934 mechanism and analogous to the observations of Martian basaltic sediments (e.g., Bristow et  
935 al., 2018): and (4) the location of elevated boron contents in illitized dioctahedral smectitic

936 clays, which may explain Martian observations (e.g., Gasda et al., 2017). The analogy may  
937 not be perfect, as the involvement of microorganisms in the alteration process of the  
938 Ediacaran Volynian flood basalts is indicated by our data, which provide another piece of  
939 evidence for the Ediacaran life on land.

940

#### 941 **Acknowledgements**

942

943 *Authors acknowledge financial support from the Polish National Science Centre*  
944 *MAESTRO grant 2013/10/A/ST10/00050, from the European Union (ERDF), and Région*  
945 *Nouvelle Aquitaine. We thank Anatoliy Makhnach for helpful discussions, Mariusz*  
946 *Paszkowski for the pyroxene separation, Malgorzata Zielińska for the clay separations,*  
947 *Zuzanna Ciesielska for collecting the XRD data, Michał Banaś for Ar isotope measurements,*  
948 *and Dorota Bakowska for K measurements. Many thanks to the State Enterprise "Ukrainian*  
949 *Geological Company" and Liubomyr Shymkiv personally, and the Republican Unitary*  
950 *Enterprise "Research and Production Center for Geology", and Alla Laptsevich and Sergei*  
951 *Mankevich personally for providing access to the core material and core descriptions. We*  
952 *also thank Valerian Ciobotaru for providing four Moldavian samples. Exceptionally thorough*  
953 *review by Elisabeth Rampe significantly improved quality of our presentation. Dennis D.*  
954 *Eberl is thanked for final polishing our English.*

955

#### 956 **References**

957

958 Alt, J. C., Honnorez, J., Laverne, C., Emmermann, R., 1986. Hydrothermal alteration of a 1  
959 km section through the upper oceanic crust, DSDP Hole 504B: mineralogy, chemistry, and  
960 evolution of seawater-basalt interactions. *Journal of Geophysical Research* 91, 10309-10335.

961

962 Alt, J.C., France-Lanord, Ch., Floyd, P. A., Castillo, P., Galy, A., 1992. Low-temperature  
963 hydrothermal alteration of Jurassic ocean crust, Site 801. In: Proceedings of the Ocean  
964 Drilling Program, Larson, R., Lancelot, Y. (Ed.), Scientific Results 129, 415-427.

965

966 Bakun-Czubarow, N., Białowolska, A., Fedoryshyn, Y., 2002. Neoproterozoic flood basalts  
967 of Zabolotta and Babino Beds of the volcanogenic Volhynian Series and Polesie Series  
968 dolerites in the western margin of the East European Craton. *Acta Geologica Polonica* 52,  
969 481-496.

970

971 Bau, M., 1991. Rare-earth element mobility during hydrothermal and metamorphic fluid-rock  
972 interaction and the significance of the oxidation state of europium. *Chemical Geology* 93,  
973 219–230.

974

975 Białowolska, A., Bakun-Czubarow, N., Fedoryshyn, Y., 2002. Neoproterozoic flood basalts  
976 of the upper beds of the Volhynian Series (East European Craton). *Geological Quarterly* 46,  
977 37–57.

978

979 Bishop, J.L., Michalski, J.R., Carter, J., 2017. Remote detection of clay minerals. In: *Infrared  
980 and Raman Spectroscopies of Clay Minerals*, Gates, W.P., Kloprogge, J.T., Madejova, J.,  
981 Bergaya F. (Eds.), *Developments in Clay Science*, 482-514.

982 Bishop, J. L., Fairén, A. G., Michalski, J. R., Gago-Duport, L., Baker, L. L., Velbel, M. A., ...  
983 & Rampe, E. B., 2018. Surface clay formation during short-term warmer and wetter  
984 conditions on a largely cold ancient Mars. *Nature Astronomy* 2(3), 206.

985

986 Blake, D.F. and 21 coauthors, 2012. Characterization and calibration of the CheMin  
987 mineralogical instrument on Mars Science Laboratory. *Space Science Reviews* 170, 341-399.  
988

989 Bobrovskiy, I., Hope, J.M., Krasnova, A., Ivantsov, A., Brocks, J.J., 2018. Molecular fossils  
990 from organically preserved Ediacara biota reveal cyanobacterial origin for *Beltanelliformis*.  
991 *Nature Ecology & Evolution*, DOI: <https://doi.org/10.1038/s41559-017-0438-6>  
992

993 Bowen, G. J., Revenaugh, J., 2003. Interpolating the isotopic composition of modern meteoric  
994 precipitation. *Water Resources Research* 39(10), 1299.  
995

996 Bristow, T. F., Rampe, E. B., Achilles, C. N., Blake, D. F., Chipera, S. J., Craig, P., ... &  
997 Grotzinger, J. P., 2018. Clay mineral diversity and abundance in sedimentary rocks of Gale  
998 crater, Mars. *Science Advances* 4(6), eaar3330.

999 Cannon, K. M., Parman, S. W., & Mustard, J. F., 2017. Primordial clays on Mars formed  
1000 beneath a steam or supercritical atmosphere. *Nature*, 552(7683), 88.

1001 Carter, J., Poulet, F., Bibring, J.P., Mangold, N., Murchie, S., 2013. Hydrous minerals on  
1002 Mars as seen by the CRISM and OMEGA imaging spectrometers: Updated global view.  
1003 *Journal of Geophysical Research Planets* 118, 831–858.  
1004

1005 Chemtob, S.M., Nickerson, N.Y., Morris, R.V., Agresti, D.G., Catalano, J.G., 2015. Synthesis  
1006 and structural characterization of ferrous trioctahedral smectites: Implications for clay mineral  
1007 genesis and detectability on Mars. *Journal of Geophysical Research Planets* 120, 1119–1140.  
1008

1009 Chukanov, N.V., Pekov, I.V., Zadov, A.E., Chukanova, V.N., Möckel, S., 2003.  
1010 Ferrosaponite  $\text{Ca}_{0.3}(\text{Fe}^{2+}, \text{Mg}, \text{Fe}^{3+})_3(\text{Si}, \text{Al})_4\text{O}_{10}(\text{OH})_2 \cdot 4\text{H}_2\text{O}$ , the new trioctahedral  
1011 smectite. *Zapiski Vserossiyskogo Mineralogicheskogo Obshchestva* 132, 68-74 (in Russian).  
1012  
1013 Cole, D.R., Ripley, E.M., 1998. Oxygen isotope fractionation between chlorite and water  
1014 from 170-350°C: A preliminary assessment based on partial exchange and fluid/rock  
1015 experiments. *Geochimica et Cosmochimica Acta* 63, 449-457.  
1016  
1017 Compston, W., Sambridge, M.S., Reinfrank, R.F., Moczyłowska, M., Vidal, G., Claesson,  
1018 S., 1995. Numerical ages of volcanic rocks and the earliest faunal zone within the Late  
1019 Precambrian of east Poland. *Journal of the Geological Society* 152, 599–611.  
1020  
1021 Craw, D., Blattner, P., Landis, C.A., 1995. Stable isotopic signatures of authigenic minerals in  
1022 a Holocene ophiolitic debris flow, Southland, New Zealand. *Clay Minerals* 30, 165-172.  
1023  
1024 Dainyak, L.G., Drita, V.A., Kudryavtsev, D.I., Simanovych, I.M., Slonimskaya, M.B., 1981.  
1025 New variety of trioctahedral smectite from effusive basalts of Tunguskaya Sineclise. *Litologia*  
1026 *i Poleznye Iskopayemye* 6, 123–129 (in Russian).  
1027  
1028 Derevska, K., Shumlyansky, V., Galetsky, L., Zagnitko, V., Pryhod'ko, V., Bezugla, M.,  
1029 Shumlyansky, L., 2006. Geological genetic model of ore-forming system and prospecting  
1030 criteria of native copper in the Volynian flood basalts. In: *Copper of the Volynian Region*,  
1031 Shumlyansky L.V. (Ed.), Logos, Kyiv, 46 – 55 (in Ukrainian).  
1032

1033 Derkowski, A., McCarty, D.K., 2017. Cesium, a water-incompatible, siloxane-complexed  
1034 cation in Earth's upper crust. *Geology* 45, 899–902.

1035

1036 Derkowski, A., Środoń, J., McCarty, D.K., 2015. Cation exchange capacity and water  
1037 content of opal in sedimentary basins: example from the Monterey Formation, California.  
1038 *American Mineralogist* 100, 1244–1256.

1039 Downs, R.T. and MSL Science Team, 2015. Determining mineralogy on Mars with the  
1040 CheMin X-ray diffractometer. *Elements* 11, 45-50.

1041 Eberl, D.D., Środoń, J., Lee, M., Nadeau, P.H., Northrop, H.R., 1987. Sericite from the  
1042 Silverton caldera, Colorado: Correlation among structure, composition, origin, and particle  
1043 thickness. *American Mineralogist* 72, 914-934.

1044 Ehlmann, B.L., Mustard, J.F., Clark, R.N., Swayze, G.A., Murchie, S.L., 2011a. Evidence for  
1045 low-grade metamorphism, hydrothermal alteration, and diagenesis on Mars from  
1046 phyllosilicate mineral assemblages. *Clays and Clay Minerals* 59, 359-377.

1047

1048 Ehlmann, B.L., Mustard, J.F., Murchie, S.L., Bibring, J-P., Meunier, A., Fraeman, A.A.,  
1049 Langevin, Y., 2011b. Subsurface water and clay mineral formation during the early history of  
1050 Mars. *Nature* 479, 53-60.

1051

1052 Eiler, J.M., 2001. Oxygen isotope variations of basaltic lavas and upper mantle rocks.  
1053 *Reviews in Mineralogy and Geochemistry* 43, 319-364.

1054

1055 Elie, M., Faure, P., Michels, R., Landais, P., Griffault L., 2000. Natural and laboratory  
1056 oxidation of low-organic-carbon-content sediments: comparison of chemical changes in  
1057 hydrocarbons. *Energy & Fuels* 14, 854-861.

1058

1059 Elie, M., Faure, P., Michels, R., Landais, P., Griffault L., Mansuy, L., Martinez, L., 2004.  
1060 Effects of water–cement solutions on the composition of organic compounds leached from  
1061 oxidized Callovo–Oxfordian argillaceous sediment. *Applied Clay Science* 26, 309-329.

1062

1063 Elming, S.Å., Kravchenko, S.N., Layer, P., Rusakov, O.M., Glevasskaya, A.M., Mikhailova,  
1064 N.P., Bachtadse, V., 2007. Palaeomagnetism and  $^4\text{ }^0\text{Ar}/^3\text{ }^9\text{Ar}$  age determinations of the  
1065 Ediacaran traps from the southwestern margin of the East European Craton, Ukraine:  
1066 relevance to the Rodinia break-up. *Journal of the Geological Society* 164, 969–982.

1067

1068 Emetz, A., Piestrzyński, A., Zagnitko, V., 2004. Geological framework of the Volhyn copper  
1069 fields with a review of the Volhyn flood basalt province (western margin of the East-  
1070 European Craton). *Annales Societatis Geologorum Poloniae* 74, 257–265.

1071

1072 Emetz, A., Piestrzyński, A., Zagnitko, V., Pryhod'ko L., Gawel A., 2006. Geology,  
1073 mineralogy and origin of Zhyrychi native copper deposit (North-Western Ukraine). *Annales*  
1074 *Societatis Geologorum Poloniae* 76, 297–314.

1075

1076 Farmer, G.L., 2003. Continental Basaltic Rocks. In: *Treatise on Geochemistry*, Elsevier,  
1077 Amsterdam, vol. 3, 85–121.

1078

1079 Faust, G.T., 1955. Thermal analysis and X-ray studies of griffithite. Journal of the  
1080 Washington Academy of Sciences 45, 66-70.  
1081

1082 Franzson, H., Zierenberg, R., Schiffman, P., 2008. Chemical transport in geothermal systems  
1083 in Iceland: Evidence from hydrothermal alteration. Journal of Volcanology and Geothermal  
1084 Research 173, 217–229.

1085 Gasda, P. J., Haldeman, E. B., Wiens, R. C., Rapin, W., Bristow, T. F., Bridges, J. C., ... &  
1086 Lanza, N. L., 2017. In situ detection of boron by ChemCam on Mars. Geophysical Research  
1087 Letters 44(17), 8739-8748.

1088 Goryl, M., Marynowski, L., 2016. Pattern of *n*-alkanes distribution characteristic for  
1089 terrestrial organic matter from the Ediacaran sedimentary rocks of the East European  
1090 Platform. Mineralogia – Special Papers 45, 57.  
1091

1092 Goryl, M., Marynowski, L., Brocks, J.J., Bobrovskiy, I., Derkowski, A., 2018. Exceptional  
1093 preservation of hopanoid and steroid biomarkers in Ediacaran sedimentary rocks of the East  
1094 European Craton. Precambrian Research 316, 38–47.  
1095

1096 Harmon, R. S., Hoefs, J., 1995. Oxygen isotope heterogeneity of the mantle deduced from  
1097 global <sup>18</sup>O systematics of basalts from different geotectonic settings. Contributions to  
1098 Mineralogy and Petrology 120, 95-114.  
1099

1100 Jambor, J.N., Roberts, A.C., 2004. New mineral names. American Mineralogist 89, 467–471.  
1101

- 1102 Juskowiak, O., Ryka, W., 1967. Volcanic and accompanying sedimentary rocks from  
1103 boreholes Kruszyniany and Mielnik. *Biuletyn Instytutu Geologicznego* 197, 69–103 (in  
1104 Polish).
- 1105
- 1106 Juskowiakowa, M., 1971. Basalts of eastern Poland. *Biuletyn Instytutu Geologicznego* 245,  
1107 175–253 (in Polish).
- 1108
- 1109 Juskowiakowa, M., 1974. Upper Precambrian sediments. *Prace Instytutu Geologicznego* 74,  
1110 20–39 (in Polish).
- 1111
- 1112 Kamiński, M., 1929. Volyn basalts. *Kosmos* 54, 675–701 (in Polish).
- 1113
- 1114 Klingelhöfer, G., Morris, R.V., Bernhardt, B., Schröder, C., Rodionov, D.S., de  
1115 -Souza, P.A., Yen, A., Gellert, R., Evlanov, E.N., Zubkov, B., and others, 2004.  
1116 Jarosite and hematite at Meridiani Planum from Opportunities Mössbauer  
1117 spectrometer. *Science* 306, 1740–1745.
- 1118
- 1119 Kohn, M.J., Valley, J.W., 1998. Oxygen isotope geochemistry of the amphiboles:  
1120 Isotope effects of cation substitutions in minerals. *Geochimica et Cosmochimica Acta*  
1121 62, 1947-1958.
- 1122
- 1123 Komadel, P., Madejová, J., Laird, D.A., Xia, Y., Stucki, J.W., 2000. Reduction of Fe(III) in  
1124 griffithite. *Clay Minerals* 35, 625–634.
- 1125
- 1126 Kremer, B., Kaźmierczak, J., Środoń, J., 2018. Cyanobacterial-algal crusts from Late

1127 Ediacaran paleosols of the East European Craton. *Precambrian Research* 305, 236-246.  
1128  
1129 Kuzmenkova, O.F., 2005. Zeolites of the Vendian basalts of Belarus. In: Proceedings of the  
1130 National Academy of Sciences of Belarus, Chemical Series 5, 158–160 (in Russian).  
1131  
1132 Kuzmenkova, O.F., 2007. Petrography of magmatic rocks of the trap formation of Belarus.  
1133 *Lithosphere* 27, 81–95. (in Russian).  
1134  
1135 Kuzmenkova, O.F., 2009. Geochemistry of the trappean formation of the Vendian of Belarus:  
1136 PhD thesis, Republican Unitary Enterprise "Belarussian Research and Exploration Institute",  
1137 Minsk, 22 pp. (in Russian).  
1138  
1139 Kuzmenkova, O.F., 2011. Material composition of the Khotislavsky copper occurrence. In:  
1140 Actual Problems of Modern Geology, Geochemistry and Geography, Materials of the  
1141 International Scientific-Practical Conference, Brest, Part 1. Geology and Geochemistry, 118–  
1142 120 (in Russian).  
1143  
1144 Kuzmenkova, O.F., Veretennikov, N.V., Nosova, A.A., Kotlyarov, V.A., 2006a. Copper  
1145 mineralization in the Vendian volcanogenic strata of Belarus. In: Copper of the Volynian  
1146 Region, Shumlyansky L.V. (Ed.), Logos, Kiyv, 171–178 (in Russian).  
1147  
1148 Kuzmenkova, O.F., Veretennikov, N.V., Samodurov, V.P., 2006b. Genesis of the analcime-  
1149 chlorophaeite-containing basalts of the Neoproterozoic (Vendian) trap formation of Belarus.  
1150 In: Volcanism and Geodynamics. Materials of the III All-Russian Symposium on  
1151 Volcanology and Paleovolcanology, Ulan-Ude, Vol. 3, 641–645 (in Russian).

1152

1153 Kuzmenkova, O.F., Nosova, A.A., Veretennikov, N.V., 2008. Mineralogy and petrogenesis of  
1154 Vendian basalts and dolerites of Belarus. *Lithosphere* 28, 76–95 (in Russian).

1155

1156 Kuzmenkova, O.F., Nosova, A. A., Shumlyansky, L.V., 2010. Comparison of Neoproterozoic  
1157 Volyn-Brest magmatic province with large world continental plate basalt provinces, the  
1158 nature of low- and high-Ti basite magmatism. *Lithosphere* 33, 3–16 (in Russian).

1159

1160 Kuzmenkova, O.F., Shumlyansky, L.V., Nosova, A.A., Voskoboynikova, T.V., Grakovich,  
1161 I.J., 2011. Petrology and correlation of trap formations of the Vendian in the adjacent areas of  
1162 Belarus and Ukraine. *Lithosphere* 35, 3–23.

1163

1164 Kvasnytsya, I., Kosovskyy, Y., Bondarenko, I., 2006. Native iron from Volyn Vendian  
1165 volcanogenic rocks. In: *Copper of the Volynian Region*, Shumlyansky L.V. (Ed.), Logos,  
1166 Kiyv, 123–131 (in Ukrainian).

1167

1168 Lazarenko, E.K., 1956. About seladonite from Volyn basalts. *Mineralny Sbornik Lvovskoho*  
1169 *Geologicheskoho Obshestva* 10, 352-362 (in Ukrainian).

1170

1171 Le Deit, L., Flahaut, J., Quantin, C., Hauber, E., Mège, D., Bourgeois, O., Gurgurewicz, J.,  
1172 Massé, M., Jaumann, R., 2012. Extensive surface pedogenic alteration of the Martian  
1173 Noachian crust suggested by plateau phyllosilicates around Valles Marineris, *Journal of*  
1174 *Geophysical Research* 117, E00J05, doi:10.1029/2011JE003983.

1175

1176 Levykh, N.N., 1999. Weathering crusts of the western part of the East European platform.  
1177 Institute of Geological Sciences, Belarussian Academy of Sciences, Minsk, 204 pp. (in  
1178 Russian).

1179  
1180 Liivamägi, S., Środoń, J., Bojanowski, M., Gerdes, A., Stanek, J. J., Williams, L., Szczerba,  
1181 M., 2018. Paleosols on the Ediacaran basalts of the East European Craton: a unique record of  
1182 paleoweathering with minimum diagenetic overprint. *Precambrian Research* 316, 66-82.

1183

1184 Madejová, J., Gates, W.P., Petit, S., 2017. IR Spectra of Clay Minerals. In: *Infrared and*  
1185 *Raman Spectroscopies of Clay Minerals*, Gates, W.P., Kloprogge, J.T., Madejova, J.,  
1186 Bergaya, F. (Eds.), *Developments in Clay Science*, Elsevier, 105-149.

1187

1188 Makhnach, A.A., Veretennikov, N.V., 1970. Volcanogenic formation of the Upper Proterozoic  
1189 (Vendian) of Belarus. *Science and Technology*, Minsk, 236 pp. (in Russian).

1190

1191 Małkowski, S., 1929. On discovery of the native copper deposit in Volyn. *Biuletyn*  
1192 *Państwowego Instytutu Geologicznego* 24, 16-17 (in Polish).

1193

1194 Marynowski, L., Wyszomirski, P., 2008. Organic geochemical evidences of early diagenetic  
1195 oxidation of the terrestrial organic matter during the Triassic arid and semi-arid climatic  
1196 conditions. *Applied Geochemistry* 23, 2612-2618.

1197

1198 Mazur, S., Porębski, S.J., Kędzior, A., Paszkowski, M., Podhalańska, T., Poprawa, P., 2018a.  
1199 Refined timing and kinematics for Baltica-Avalonia convergence based on the sedimentary  
1200 record of a foreland basin. *Terra Nova* 30, 1-8.

1201 Mazur, S., Krzywiec, P., Malinowski, M., Lewandowski, M., Aleksandrowski, P.,  
1202 Mikołajczak, M., 2018b. On the nature of the Teisseyre-Tornquist Zone. *Geology,*  
1203 *Geophysics and Environment* 44, 17–30.

1204

1205 Melnychuk, V.G., 2006. Hydrothermal mineralogical zonality and metamorphism in copper-  
1206 bearing Vendian flood basalts of the Volyno-Podolian plate. In: *Copper of the Volynian*  
1207 *Region*, Shumlyansky L.V. (Ed.), Logos, Kiyv, 131 – 142 (in Ukrainian).

1208

1209 Mysiak, I.M., Skakun, L.Z., Serkiz, R.Y., 2016. Unusual association of native metals in the  
1210 platobasalts of Volyn and conditions of their formation. *Mineralogical Journal (Ukraine)* 38,  
1211 14-22 (in Ukrainian).

1212

1213 Nawrocki, J., Poprawa, P., 2006. Development of Trans-European Suture Zone in Poland:  
1214 from Ediacaran rifting to Early Palaeozoic accretion. *Geological Quarterly* 50, 59-76.

1215

1216 Nehring-Lefeld, M., Modlinski, Z., Swadowska, E., 1997. Thermal evolution of the  
1217 Ordovician in the western margin of the East-European Platform: CAI and  $R_0$  data.  
1218 *Geological Quarterly* 41, 129–138.

1219

1220 Nosova, A.A., Kuzmenkova, O.F., Veretennikov, N.V., Petrova, L.G., Levsky, L.K., 2008.  
1221 Neoproterozoic Volhynia-Brest magmatic province in the western East European Craton:  
1222 withing-plate magmatism in ancient suture zone. *Petrology* 16, 105–135 (in Russian).

1223

- 1224 Paczeńska, J., 2010. The evolution of late Ediacaran riverine-estuarine system in the Lublin-  
1225 Podlasie slope of the East European Craton, southeastern Poland. Polish Geological Institute  
1226 Special Papers 27, 1–96.  
1227
- 1228 Peacock, M.A., Fuller, R.E., 1928. Chlorophaeite, sideromelane and palagonite from the  
1229 Columbia River Plateau. *American Mineralogist* 13, 369-382.  
1230
- 1231 Pehr, K., Love, G.D., Kuznetsov, A., Podkovyrov, V., Junium, C.K., Shumlyansky, L.,  
1232 Sokur, T., Bekker, A., 2018. Ediacara biota flourished in oligotrophic and bacterially  
1233 dominated marine environments across Baltica. *Nature Communications* 9, 1807. DOI:  
1234 <https://doi.org/10.1038/s41467-018-04195-8>
- 1235 Poprawa, P., Šliaupa, S., Stephenson, R., Lazauskiene, J., 1999. Late Vendian–Early  
1236 Palaeozoic tectonic evolution of the Baltic Basin: regional tectonic implications from  
1237 subsidence analysis. *Tectonophysics* 314, 219-239.  
1238
- 1239 Rajchel, J., 2012. Antique cobblestone pavement in Krakow. *Brukbiznes* 3, 18-23 (in Polish).  
1240
- 1241 Robinson, D., Schmidt, S.Th., Santana De Zamora, A., 2002. Reaction pathways and reaction  
1242 progress for the smectite-to-chlorite transformation: evidence from hydrothermally altered  
1243 metabasites. *Journal of Metamorphic Geology* 20, 167-174.  
1244
- 1245 Rollinson, H.R., 1994. *Using Geochemical Data: Evaluation, Presentation, Interpretation.*  
1246 Longman Scientific & Technical, 352 pp.

- 1247 Ross, C.S., 1960. Review of the relationships in the montmorillonite group of clay minerals.  
1248 Clays and Clay Minerals. Proceedings of the Seventh National Conference on Clays and Clay  
1249 Minerals, 225-229.
- 1250 Rouxel, O., Dobbek, N., Ludden, J., Fouquet, Y., 2003. Iron isotope fractionation during  
1251 oceanic crust alteration. *Chemical Geology* 202, 155–182.  
1252
- 1253 Rybicki, M., Marynowski, L., Misz-Kennan, M., Simoneit, B.R.T., 2016. Molecular tracers  
1254 preserved in Lower Jurassic “Blanowice brown coals” from southern Poland at the onset of  
1255 coalification: Organic geochemical and petrological characteristics. *Organic Geochemistry*  
1256 102, 77–92.  
1257
- 1258 Sarkar, P.K., Upasani, D.V., Wani, V., 2016. Alteration of volcanic glass to well-crystallized  
1259 ferrosaponite in the vesicles of the Deccan trap basalts at Bhuleshwar Ghat section, Pune  
1260 district, Maharashtra. *Journal of the Geological Society of India* 88, 22–28.
- 1261 Savin, S.M., Lee, M., 1988. Isotopic studies of phyllosilicates. *Reviews in Mineralogy* 19,  
1262 189–223.
- 1263 Schmidt, S.Th., 1993. Regional and local patterns of low-grade metamorphism in the North  
1264 Shore Volcanic Group, Minnesota, USA. *Journal of Metamorphic Geology* 11, 401-414.

1265 Schmidt, S.Th., Robinson, D., 1997. Metamorphic grade and porosity and permeability  
1266 controls on mafic phyllosilicate distributions in a regional zeolite to greenschist facies  
1267 transition of the North Shore Volcanic Group, Minnesota. *GSA Bulletin* 109, 683-697.

1268 Shau, Y-H., Peacor, D.R., 1992. Phyllosilicates in hydrothermally altered basalts from DSDP  
1269 Hole 504B, Leg 83 — a TEM and AEM study. *Contributions to Mineralogy and Petrology*  
1270 112, 119–133.

1271

1272 Sheppard, S.M.F., Gilg, H.A., 1996. Stable isotope geochemistry of clay minerals. *Clay*  
1273 *Minerals* 31, 1-24.

1274

1275 Shumlyanskyy, L.V. (Ed.), 2006. Copper of the Volynian Region. Logos, Kiyv (in Russian  
1276 and Ukrainian).

1277

1278 Shumlyanskyy, L.V., Tsymbal, S.M., 2006. On the character of secondary alteration of  
1279 volcanogenic rocks of the Volynian flood basalt province. In: Shumlyanskyy L.V.V. (Ed.),  
1280 Copper of the Volynian Region. Logos, Kiyv, 56 – 66 (in Ukrainian).

1281

1282 Shumlyanskyy, L.V., Nosova, A., Billstrom K., Soderlund U., Andreasson, P.G.,  
1283 Kuzmenkova, O., 2016. The U-Pb zircon and baddeleyite ages of the Neoproterozoic Volyn  
1284 Large Igneous Province: implication for the age of the magmatism and the nature of a crustal  
1285 contaminant. *GFF* 138, 17–30.

1286

1287 Simanovich, I.M., Drits, V.A., Dainyak, L.G., 1986. Smectites and isotropic phases in basalts  
1288 of northern Timan. *Lithology and Mineral Resources* 1, 86 – 103 (in Russian).

1289

1290 Simanovich, I.M., Yapaskurt, O.V., Gorbachev, V.I., 2010. Trap magmatism and  
1291 mobilization of hydrocarbon fluids (Western Siberia). Moscow University Geology Bulletin  
1292 65, 153-160.  
1293

1294 Skakun L., Tkachuk A., Melnychuk V. 2006. Formation of zeolite mineralization in the  
1295 hydrothermal rocks of of the flood basalts of Volynian series. In: Copper of the Volynian  
1296 Region, Shumlyansky L.V.V. (Ed.), Logos, Kiyv, 71 – 81 (in Ukrainian).  
1297

1298 Środoń, J., 2010. Evolution of boron and nitrogen content during illitization of bentonites.  
1299 Clays and Clay Minerals 58, 743-756.  
1300

1301 Środoń, J., Clauer, N., Eberl, D.D., 2002. Interpretation of K-Ar dates of illitic clays from  
1302 sedimentary rocks aided by modelling. American Mineralogist 87, 1528-1535.  
1303

1304 Środoń J., Zeelmaekers E., Derkowski A., 2009. The charge of component layers of illite-  
1305 smectite in bentonites and the nature of end-member illite. Clays & Clay Minerals 57, 649–  
1306 671.  
1307

1308 Stone, C., Fan, P., 1978. Hydrothermal alteration of basalts from Hawaii Geothermal Project  
1309 Well-A, Kilauea, Hawaii. Geology 6, 401-404.  
1310

1311 Stroncik, N.A., Schmincke, H-U., 2002. Palagonite – a review. International Journal of Earth  
1312 Sciences (Geologische Rundschau) 91, 680–697.  
1313

1314 Sun, S.-s., McDonough, W.F., 1989. Chemical and isotopic systematics of oceanic basalts:  
1315 implications for mantle composition and processes. Geological Society Special Publication  
1316 42, 313–345.

1317

1318 Teutsch, N., Schmid, M., Müller, B., Halliday, A.N., Bürgmann, H., Wehrli, B., 2009. Large  
1319 iron isotope fractionation at the oxic–anoxic boundary in Lake Nyos. Earth and Planetary  
1320 Science Letters 285, 52–60.

1321

1322 Treiman, A. H., Morris, R. V., Agresti, D. G., Graff, T. G., Achilles, C. N., Rampe, E. B., ...  
1323 & Bish, D. L., 2014. Ferrian saponite from the Santa Monica Mountains (California, USA,  
1324 Earth): Characterization as an analog for clay minerals on Mars with application to  
1325 Yellowknife Bay in Gale Crater. American Mineralogist 99, 2234-2250.

1326

1327 Ushakova, Z.G., 1962. Lower Paleozoic trap formation in western part of the Russian  
1328 platform. WSEGEI Works (Труды ВСЕГЕИ) 30, 108 pp. (in Russian).

1329

1330 Vaniman, D. T., Bish, D. L., Ming, D. W., Bristow, T. F., Morris, R. V., Blake, D. F., ... &  
1331 Rice, M., 2014. Mineralogy of a mudstone at Yellowknife Bay, Gale crater,  
1332 Mars. Science, 343(6169), 1243480.

1333

1334 Weill, D.F., Drake M.J., 1973. Europium anomaly in plagioclase feldspar: experimental  
1335 results and semiquantitative model. Science 180, 1059–1060.

1336

1337 Wu, L., Beard, B.L., Roden, E.E., Kennedy, C.B, Johnson, C.M., 2010. Stable Fe isotope  
1338 fractionations produced by aqueous Fe(II)-hematite surface interactions. *Geochimica et*  
1339 *Cosmochimica Acta* 74, 4249-4265.

1340

1341

1342 **Tables**

1343 Table 1. Decomposition of Mössbauer spectra of rocks and selected clay fractions, % Fe<sup>2+</sup> in  
1344 total Fe calculated from the decomposition data for bulk rock and clay fraction, oxygen and  
1345 iron isotope data, along with % primary minerals from Supplementary Table 1.

1346

1347 Table 2. Chemical composition (wt% SEM/EDS microchemical analyses) of isotropic  
1348 chlorophaeite and replacing birefringent smectitic clays in different sites of the basaltic rock  
1349 affected by incipient alteration (sample 4522-1). Ferrous state has been assigned to iron in all  
1350 analyses.

1351

1352 Table 3. K-Ar data for selected clay fractions containing aluminoceladonite and/or illite-  
1353 smectite (cf. Supplementary Table 3).

1354

1355 Table 4. Structural formulae of smectites from Volynian basalts, presented along with  
1356 formulae derived from published chemical data of similar materials: griffithite from Ross  
1357 (1960) and Komadel et al. (2000), oxysmectites from Dainyak et al. (1981), and ferrosaponite  
1358 from Jambor et al. (2004). Formula of chlorite (Kob-23) added to show tendency in chemical  
1359 composition of clays.

1360

1361 Table 5. Characteristics of end-member di- and trioctahedral smectite from Volynian basalts  
1362 extrapolated using number of atoms in the octahedral sheet given in Table 4.

1363

1364 Supplementary Table 1. Quantitative XRD mineral composition data for basalts, green clays  
1365 from veins and cavities in basalt, and rhyodacites, plus XRD estimates of chlorophaeite  
1366 composition. Basalts arranged by alteration steps I-V, based on sum of primary minerals. If  
1367 data available, basalts are assigned to lower or upper volcanic series.

1368

1369 Supplementary Table 2. Quantitative XRD mineral composition data for tuffs and for basalt-  
1370 tuff alternation in section Kobryn. Tuffs arranged from felsic to basic, based on the content of  
1371 quartz. If data available, samples are assigned to lower or upper volcanic series.

1372

1373 Supplementary Table 3. Mineral composition of  $<0.2 \mu\text{m}$  fractions, separated from basalts,  
1374 green clays in veins and cavities, and tuffs. The peak position data, used in the evaluation of  
1375 percent smectite layers (%S) in illite-smectite are given along with calculated %S and the  
1376 average %S value. tr: trace, i-s: illite-smectite, ch-s: chlorite-smectite,  $\delta 2$ : angular distance  
1377 between i-s reflections in  $42\text{-}49^\circ 2\theta$  range.

1378

1379 Supplementary Table 4. Chemical composition of basalts, chlorophaeite, green clays from  
1380 veins and cavities in basalt, rhyodacites, tuffs, and clay fractions. Major elements and loss on  
1381 ignition (LOI) given in %, trace elements in ppm. Below average values for different  
1382 lithologies and compositions of clay fractions along with their bulk rocks are listed.

1383

1384 **Figure captions**

1385

1386 Figure 1. Map of the Volyn-Brest volcanic province with sampling sites indicated (modified  
1387 from Kuzmenkova et al., 2010, TTZ after Mazur et al., 2018b).

1388

1389 Figure 2. Random powder XRD patterns of the bulk rock, with ZnO internal standard,  
1390 illustrating the compositional variability of Volyn basalts, reflecting the degree of  
1391 hydrothermal alteration.

1392

1393 Figure 3. Random powder XRD patterns of the chlorophaeite accumulations, registered in  
1394 glass tubes because of the scarcity of the available material, and documenting coexistence of  
1395 di and trioctahedral smectite (02 peaks at 4.48 and 4.58 Å, respectively).

1396

1397

1398 Figure 4.  $^{57}\text{Fe}$  room temperature Mössbauer spectra of bulk rock basalts, chlorophaeite  
1399 (Mokrany-3A), chloritic clay in basalt (Kob-23), and tuffs (B), illustrating the variability of  
1400 compositions encountered, and presented along with calculated spectra of iron-bearing  
1401 fractions used in the fitting procedure.

1402

1403 Figure 5. FTIR transmission KBr spectra (<0.2  $\mu\text{m}$  fraction) of basaltic clays: Mokrany-3B  
1404 and 4504-1A, with end-member components used as references: chlorite (Kob-23),  
1405 trioctahedral smectite (4600-1), and dioctahedral smectite from paleosol (4517-1); Qz: quartz  
1406 (distinctive bands).

1407

1408 Figure 6. FTIR transmission KBr spectra of chlorophaeite accumulations (a) and surrounding  
1409 basalts (b); Qz: quartz (distinctive bands), Pl: feldspars (distinctive bands).

1410

1411 Figure 7. Partial  $m/z$  71 mass chromatogram for TMS derivatized basalt extract showing the  
1412 odd-over-even long chain  $n$ -alkanes predominance (A) and partial  $m/z$  117 mass  
1413 chromatograms showing comparison of  $n$ -alkanoic acids for unaltered basalt (4600-3B) and  
1414 cavity clay (4600-3A). Note high-molecular-weight  $n$ -alkanoic acids (26 to 32) in the basalt  
1415 sample (B). Numbers denote carbon atoms in the molecule.

1416

1417 Figure 8. Photomicrographs (optical microscopy) and SEM images (BSE mode) of isotropic  
1418 chlorophaeite (A-D) and its smectitic alteration products (E-H). (A) Intersertal chlorophaeite  
1419 through the body of the basaltic rocks (sample 4522-1). (B) Chlorophaeite with collomorph  
1420 texture coating the wall of circular cavities (sample 4522-1). (C) chlorophaeite pseudomorphs  
1421 after orthopyroxene (sample 4603-1). (D) Chlorophaeite as veinlet and filling product of  
1422 diktytaxitic voids in the wall-rock (sample 4522-1). (E) Incipient alteration of chlorophaeite at  
1423 the contact of a plagioclase microlite (sample 4522-1). (F) Details of the clay-rich  
1424 microspherules related to incipient alteration of chlorophaeite (sample 4522-1). (G) Strong  
1425 replacement of chlorophaeite, partial replacement of chlorite and local dissolution of quartz  
1426 filling a vesicle in a moderately altered basalt (sample 4519-0). (H) Morphological aspects of  
1427 the smectitic clays as a function of alteration sites (sample 4519-0). Microspherules  
1428 predominate in both altered chlorophaeite and chlorite while ribbon like morphology is  
1429 observed when alteration is developed at the contact between quartz and chlorophaeite. Am:  
1430 fresh chlorophaeite; Ze: zeolite; OPXps: chlorophaeite pseudomorph after orthopyroxene;  
1431 CPX: clinopyroxene; Pl: plagioclase; Ma: magnetite; Amv: chlorophaeite veinlet; Sm  
1432 smectitic clays; IRL: iron-rich layer; AH: alteration halo; Ch: iron rich chlorite; Qz: quartz.

1433

1434 Figure 9.

1435 Relationship between % clay from XRD and % MgO (red triangles) and % LOI (loss on  
1436 ignition) in basalts of variable degree of alteration. The LOI trend (blue diamonds)  
1437 extrapolates to a value intermediate between rocks dominated by chlorite and smectite (pink  
1438 squares).

1439

1440

1441 Figure 10. Primitive mantle normalized REE spectra of basalts with variable degree of  
1442 alteration, chlorophaeite, vein clay (Fe-saponite), and rhyodacites.

1443

1444 Figure 11. Relationship between % primary minerals from XRD and  $\delta^{18}\text{O}_{\text{VSMOW}}$  in basalts of  
1445 variable degree of alteration, chlorophaeite accumulation, clay veins, and basaltic tuffs.

1446

1447 Figure 12. The oxygen isotope compositional ranges of smectites from paleosols, basalt, and  
1448 green clay veins in basalt from this study plotted onto the relationship of equilibrium oxygen  
1449 isotope fractionation between smectite and water as a function of temperature based the  
1450 equation of Sheppard and Gilg (1996).

1451

1452 Figure 13. Relationship between % primary minerals from XRD and percent divalent iron in  
1453 total iron of basalts with variable degree of alteration, of their clay fractions, and of the  
1454 chlorophaeite sample Mokraný-3A.

1455

1456 Figure 14. A synthetic model of basalt alteration during the hydrothermal episode, presenting  
1457 the most important changes in mineral and chemical composition (details in the text). Pl -  
1458 plagioclase, Py - pyroxene, M - magnetite+pseudobrookite+ilmenite, Z - zeolites, Ch -

1459 chlorite, A - anatase, H - hematite, Ksp - K-feldspar, Q -quartz, Tri-S - Fe-saponite, Di-S - Fe-  
1460 montmorillonite.

1461

1462

1463 Inline Supplementary Figure 1. Random powder XRD patterns of the bulk rock, with ZnO  
1464 internal standard, illustrating the compositional variability of Volyn tuffs, from felsic (top) to  
1465 basic (bottom), with rhyodacite Skv-0C as reference.

1466

1467 Inline Supplementary Figure 2. Oriented glycolated XRD patterns of <0.2  $\mu\text{m}$  clay fractions  
1468 (with  $\text{MoS}_2$  as internal standard), representative for the variability encountered in basalts and  
1469 green clays from veins and cavities in basalt.

1470

1471 Inline Supplementary Figure 3. Random powder XRD patterns of <0.2  $\mu\text{m}$  basalt clay  
1472 fractions and <2  $\mu\text{m}$  fraction of griffithite, documenting coexistence of di- and trioctahedral  
1473 smectite. The reference griffithite sample from Griffith Park, California, was provided by Dr.  
1474 Jana Madejova.

1475

1476 Inline Supplementary Figure 4. Oriented glycolated XRD patterns of <0.2  $\mu\text{m}$  clay fractions,  
1477 representative for the variability encountered in tuffs.

1478

1479 Inline Supplementary Figure 5.  $^{57}\text{Fe}$  room temperature Mössbauer spectra of minerals, used  
1480 for decomposing spectra of bulk rocks (results of decomposition in Table 1).

1481 Inline Supplementary Figure 6. Relationship between % plagioclase from XRD and % CaO in  
1482 basalts of variable degree of alteration. Three samples off the general trend (blue diamonds)  
1483 contain calcite veinlets.

1484

1485

1486 Inline Supplementary Figure 7. Relationship between % dioctahedral clays from XRD and  
1487 ppm boron in basalts of variable degree of alteration.

1488

1489 Inline Supplementary Figure 8. Relationship between %  $K_2O$  calculated from XRD contents  
1490 of K-feldspar (assuming 12%  $K_2O$ ) and dioctahedral clay (6%  $K_2O$ ) and measured %  $K_2O$  in  
1491 basalts of variable degree of alteration.

1492

1493 Inline Supplementary Figure 9. Relationship between %  $P_2O_5$  and ppm LREE in bulk rocks.

1494

1495 Inline Supplementary Figure 10. Quantitative evolution of secondary minerals in the course of  
1496 basalt hydrothermal alteration traced by percent of primary minerals.

1497

1498 Inline Supplementary Figure 11. Differentiation of tuffs into felsic (close to rhyodacite) and  
1499 basaltic, based on quartz and K-feldspar XRD contents.

1500

1501 Inline Supplementary Figure 12. Chemical variability of tuffs (felsic vs. basaltic) traced using  
1502 the most immobile trace elements.

1503

1504 Inline Supplementary Figure 13. Chemical differences between basalts and tuffs illustrated  
1505 for a single profile (Kobryn) using the most immobile trace elements.

1506

Sample	Hematite	Magnetite	Ill-sm	Saponite	Saponite	Chlorite	Pyroxene	%Fe <sup>2+</sup> in	%Fe <sup>2+</sup> in	δ <sup>18</sup> O		Fe isotopes in <0.2 μm fraction				% primary minerals
	3+	3+ & 2+	3+	3+	2+	2+	2+	bulk rock Fe	clay Fe	Bulk rock	< 0.2	δ <sup>56</sup> Fe	2 SD	δ <sup>57/54</sup> Fe	2 SD	
<b>Basalts arranged by % primary minerals</b>																
4522-1	0	35	0	12*	0	0	53	65	0	8,1						93
Novosiolki-1	0	31	0	16	0	0	52	62	0	5,6						91
Skv-0A	0	24	5	18	0	0	44	52	0	8,4						85
Skv-0B	0	25	0	25*	3	0	47	58	11							85
Mokrany-1B	0	38	0	20*	0	0	33	46	0	6,8						79
Kob-13	0	27	0	28	8	0	38	55	22	10,8						74
Kob-14	6	21	0	28	11	16	19	53	49	9,9						66
4603-1	0	28	14	29	0	0	29	38	0	11,6						64
4504-1A	1	44	2	19	7	0	27	49	25	11,1						58
4504-1A < 0.2	0		34	41	25	0			25		17,8	-0,204	0,044	-0,305	0,055	
4466-1	9	56	12	6	0	0	18	37	50	12,6						53
Mokrany-3B	2	24	25	33	7	0	8	23	11	16,4						41
Mokrany-3B < 0.2	0		38	49	10	3			13		21	0,028	0,035	0,040	0,047	
Kob-15	11	21	0	24	44	0	0	51	65							31
4417-1	28	33	5	12	21	0	0	32	55							25
4417-1 < 0.2	20		29	20	19	12			39		18,3	-0,025	0,039	-0,072	0,059	
4600-1	15			39	46	0	0	46	54	17						7
4600-1 < 0.2	0		0	58	42	0			42		14,7	-0,459	0,060	-0,735	0,076	
Kob-23	0	0	0	5	0	95	0	95	95	10,1		-0,574	0,055	-0,843	0,066	0
<b>Chlorophaeite accumulations</b>																
Mokrany-3A	0	0	40	43	17	0	0	17	17	23						0
<b>Tuffs arranged by % quartz</b>																
Pinsk-50	15	0	40	0	44	0	0	44	52	15,2						
Pinsk-44	8	0	43	0	0	50	0	50	54	13,4						
Pinsk-47D	22	0	38	0	39	0	0	39	51	14,6						
Kob-16	30	9	34	0	28	0	0	31	45							
4600-2A	47	0	15	20	0	17	0	17	33	15						
Pinsk-47A	15	10	39	0	35	0	0	38	47	15,5						
Tashki-10	45		28	15	11	0		11	21	20	18,3					
<b>Paleosols</b>																
4529-2											21,3					
4517-1											21,7					

1507

1508 Table 1. Decomposition of Mössbauer spectra of rocks and selected clay fractions, % Fe<sup>2+</sup> in

1509 total Fe calculated from the decomposition data for bulk rock and clay fraction, oxygen and

1510 iron isotope data, along with % primary minerals from Supplementary Table 1.

1511

1512 Table 2. Chemical composition (wt% SEM/EDS microchemical analyses) of isotropic  
 1513 chlorophaeite and replacing birefringent smectitic clays in different sites of the basaltic rock  
 1514 affected by incipient alteration (sample 4522-1). Ferrous state has been assigned to iron in all  
 1515 analyses.

1516

1517

Petrographic entity	Na <sub>2</sub> O	MgO	Al <sub>2</sub> O <sub>3</sub>	SiO <sub>2</sub>	K <sub>2</sub> O	CaO	TiO <sub>2</sub>	MnO	FeO	S
Isotropic chlorophaeite	0,49	2,96	5,61	48,41	0,56	1,75	0,06	0,14	22,63	8
	0,45	2,84	5,89	49,39	0,54	1,79	0,11	0,15	22,54	8
	0,3	3,31	6,05	50,17	0,54	2	0,07	0,19	23,65	8
Smectite	0,32	4,54	8,23	47,69	0,4	1,96	0,16	0,13	19,34	8
	0,09	4,25	9,73	46,23	0,87	1,81	0,34	0,13	16,45	7
	0,21	4,91	9,78	49,83	0,54	1,91	0,34	0,15	17,69	8

1518

1519

1520 Table 3. K-Ar data for selected clay fractions containing aluminoceladonite and/or illite-  
 1521 smectite (cf. Supplementary Table 3).

1522

1523

Sample and fraction	Mass [mg]	% K <sub>2</sub> O	% K	% 40Ar*	Age [Ma]	Error [Ma]	Ave. age [Ma]	Ave. error [Ma]
Kob-9B 2-0.2µm	10,50	7,395	6,139	95,7	446,7	11,7	448,5	8,3
	8,86			95,8	450,3	11,8		
Kob-9B <0.2µm	10,91	7,355	6,105	91,4	452,2	12,0	451,1	8,4
	8,93			97,1	449,9	11,8		
Vilch19 <0.2µm	10,91	4,115	3,416	93,6	442,7	13,1	439,4	9,3
	8,34			90,6	436,1	13,1		
Ochryny21 2-0.2µm	6,97	2,885	2,395	84,5	430,6	15,8	432,6	11,1
	7,71			94,3	434,6	15,6		
Ochryny-21 <0.2µm	8,45	3,74	3,105	96,3	420,2	13,1	419,2	9,4
	5,92			96,4	418,2	13,3		
Tashki1 2-0.2µm	8,66	1,785	1,482	89,2	298,2	19,9	297,1	14,1
	10,07			76,2	296,1	19,9		
Tashki-1 <0.2µm	10,81	2,07	1,718	92,9	310,9	16,3	309,0	11,4
	9,02			94,9	307,2	15,9		

1524

1525

1526 Table 4. Structural formulae of smectites from Volynian basalts, presented along with  
 1527 formulae derived from published chemical data of similar materials: griffithite from Ross  
 1528 (1960) and Komadel et al. (2000), oxysmectites from Dainyak et al. (1981), and ferrosaponite  
 1529 from Jambor et al. (2004). Formula of chlorite (Kob-23) added to show tendency in chemical  
 1530 composition of clays.

1531

1532

Sample	Mokransky-3B < 0.2	4504-1A < 0.2	4600-1 < 0.2	Ross griffithite	Komadel griffithite	Oceanic oxysmectite	Continental oxysmectite	Ferrosaponite	Kob-23 bulk
Fraction Fe <sup>3+</sup>	0,87	0,75	0,56	0,46	0,91	0,54	0,83	0,25	0,00
Si	3,90	3,47	3,21	3,17	3,34	3,40	3,23	2,91	3,57
Al <sup>IV</sup>	0,10	0,53	0,75	0,83	0,66	0,59	0,47	1,03	0,43
Fe <sup>IV</sup>	0,00	0,00	0,04	0,00	0,00	0,01	0,30	0,06	0,00
Al <sup>VI</sup>	0,50	0,16	0,00	0,03	0,06	0,00	0,00	0,00	1,04
Fe <sup>3+</sup>	0,60	0,54	0,44	0,44	0,75	0,56	1,10	0,52	0,00
Fe <sup>2+</sup>	0,09	0,18	0,35	0,52	0,07	0,47	0,22	1,56	2,63
Mg	1,11	1,81	2,18	1,88	1,82	1,78	1,27	0,87	1,96
Layer charge	-0,38	-0,47	-0,42	-0,61	-0,46	-0,44	-0,50	-0,67	-0,13
No. oct. cat.	2,31	2,68	2,97	2,87	2,70	2,80	2,59	2,95	5,63
Ca	0,01	0,07	0,01	0,25	0,01	0,06	0,21	0,31	0,03
Na	0,32	0,32	0,38	0,11	0,43	0,31	0,05	0,04	0,08
K	0,04	0,01	0,02	0,00	0,01	0,02	0,03	0,01	0,01
Mg	0,00	0,00	0,00	0,00	0,00	0,00	0,00	0,00	0,00
NH <sub>4</sub>	0,00	0,00	0,00	0,00	0,00	0,00	0,00	0,00	0,00
Interlayer charge	0,38	0,47	0,42	0,61	0,46	0,44	0,50	0,67	0,15
Si/(Si+Al)	0,87	0,83	0,81	0,79	0,82	0,85	0,87	0,74	0,71
Fe/(Mg+Fe)	0,38	0,29	0,27	0,34	0,31	0,37	0,56	0,71	0,57

1533

1534

1535 Table 5. Characteristics of end-member di- and trioctahedral smectite from Volynian basalts

1536 extrapolated using number of atoms in the octahedral sheet given in Table 4.

1537

1538

Smectite	di	tri
Si	4,00	3,16
Al <sup>VI</sup>	0,72	0,00
Fe <sup>3+</sup>	0,68	0,44
Fe <sup>2+</sup>	0,00	0,34
Mg	0,64	2,27
$\delta^{18}\text{O}$	24,0	14,5
$\delta^{56}\text{Fe}$	0,27	-0,47
ppm LREE	664,00	0,00
ppm HREE	27,00	4,00

1539

1540

1541 **Supplementary Materials**

1542 ***Experimental methods***

1543 ***QXRD of the bulk rock***

1544           The mineral composition of whole rock samples was studied by means of quantitative  
1545 X-ray diffractometry (QXRD). A 3 g sample was spiked with 10% ZnO, ground in the  
1546 McCrone mill with methanol, and a randomly oriented preparation was made by side-loading  
1547 (Środoń et al., 2001). The XRD patterns were recorded in 2–65° 2θ CuKα range with  
1548 0.02°/sec step on Thermo X'tra diffractometer, the mineral phases were identified and then  
1549 quantified using QMIN software (by Dr. Marek Szczerba), which matches the sum of the  
1550 diffraction patterns of pure mineral standards with the pattern of a studied rock sample,  
1551 allowing for manual corrections. Dioctahedral and trioctahedral clays were quantified as  
1552 groups by careful 060 reflection fitting (Środoń et al., 2001) and split into species by fitting  
1553 the peaks in the 17–35° 2θ range. Chlorophaeite samples, available in quantities too small to  
1554 conduct regular QXRD, were analyzed only qualitatively in glass capillaries in 4-39°  
1555 2θ range, as random powders without the spike.

1556           QMIN software does not provide errors of mineral phase determination. Uncertainty  
1557 of the QXRD analysis can be however evaluated from the results of Reynolds Cup –  
1558 quantitative mineral analysis international round robin (Raven and Self, 2017). We got 4<sup>th</sup>  
1559 place in 2018 Reynolds Cup, with the absolute error per major components of 2.4%.  
1560 Considering much simpler mineralogy of the samples analyzed in this study than of the  
1561 samples of Reynolds Cup, the uncertainty of QXRD measurements should be even smaller.

1562

1563 ***Clay fraction separation***

1564           The clay fractions 2-0.2 and <0.2 μm were separated from ca. 50 g of the bulk rock after  
1565 ultrasonic dispersion of the crushed rock in deionized water. Standard chemical treatments  
1566 (Jackson, 1975) were used for samples prepared for K-Ar dating, but they were avoided in  
1567 case of the Mössbauer and FTIR studies, in order to minimize the oxidation of structural iron.

1568 The fractions were collected by centrifugation, coagulation by adding concentrated NaCl  
1569 solution, dialysis, and freeze-drying.

#### 1570 *XRD of clay fraction*

1571 Clay mineral identification in the bulk rock was verified and made more accurate by  
1572 studying 2-0.2 and <0.2  $\mu\text{m}$  fractions of selected samples. XRD patterns were recorded in air-  
1573 dried and glycolated state of the oriented slides, prepared by sedimentation of 10 mg clay/cm<sup>2</sup>  
1574 from a sonified water suspension, with 4% MoS<sub>2</sub> as the internal standard. The collected XRD  
1575 patterns were first analyzed using Mering rules for the identification of clay minerals (Moore  
1576 and Reynolds, 1997) and then percent smectite layers in mixed-layer illite-smectite (%S) was  
1577 measured from the selected peak positions on glycolated patterns, using the regressions based  
1578 on data of Środoń et al. (2009).

#### 1579 *K-Ar dating of illite*

1580 Na-exchanged, 2.0–0.2 and <0.2  $\mu\text{m}$  clay fractions containing illite-smectite and  
1581 aluminoceladonite were dated by K-Ar method to establish the age of crystallization of these  
1582 minerals. All the measurements were performed at the Institute of Geological Sciences, Polish  
1583 Academy of Sciences in Kraków using Nu Instruments Noblesse multicollector noble-gas  
1584 spectrometer. Four portions of samples: two 10 mg and two 50 mg, were weighted using  
1585 Sartorius mass balance with precision of 0.01 mg. A small quantity of CuO (approximately  
1586 0.1 mg) was added to the two lightest portions. These samples were then wrapped in an Al-  
1587 foil and proceeded to radiogenic argon measurements. Two heaviest portions were weighted  
1588 directly on platinum evaporators and proceeded to potassium measurements. All the samples  
1589 were equilibrated in the ambient atmosphere (air-dry state) and weighted one after another in  
1590 order to minimize the errors due to relative humidity affecting clay hydration.

1591 Radiogenic argon measurements were performed on Nu Instruments Noblesse  
1592 multicollector noble-gas spectrometer (NG039). The spectrometer is equipped with a Nier-  
1593 type ion-source, 75° magnetic sector, two quadrupole lenses and a collector block. The  
1594 collectors assembly consists of a Faraday detector (FAR) and three ETP ion-counting electron  
1595 multipliers (IC0, IC1, IC2). The high mass isotope (<sup>40</sup>Ar) is switchable between Faraday and  
1596 IC0 multiplier, depending on the height of the measured signal. Due to high mass resolving  
1597 power (MRP), which is ~5400, it is possible to resolve combined peaks of <sup>36</sup>Ar + H<sup>35</sup>Cl from

1598 peaks of  $^{36}\text{Ar} + \text{H}^{35}\text{Cl} + ^{12}\text{C}_3$ . The signal of all argon isotopes was always calculated as a  
1599 difference between measurement for sample and signal measured directly before, when ion  
1600 pump was pumping the interior of the spectrometer. It was done to correct for background  
1601 level of  $^{36}\text{Ar} + \text{H}^{35}\text{Cl}$ ,  $^{38}\text{Ar} + \text{H}^{37}\text{Cl}$  and also of  $^{40}\text{Ar}$  that is always leaking in very small  
1602 quantities to the spectrometer through gaskets (background signal was at around 60, 40 and  
1603 400 cps, respectively; while e.g. for GL-O it is at: ~2000, ~30000, ~5000000 cps,  
1604 respectively). Amount of  $^{35}\text{Cl}$  was also always monitored prior to the sample and when the  
1605 sample was being measured: differences are maximally of few percent. This indirectly  
1606 indicates that level of  $\text{H}^{35}\text{Cl}$  was constant prior and during measurements and, considering  
1607 very low background level of  $^{36}\text{Ar} + \text{H}^{35}\text{Cl}$  peak, the used correction was reasonable.

1608 Extraction-purification line with all-metal valves is attached to the Noblesse  
1609 spectrometer. The Al-foil wrapped portions were loaded into a glass container, which is a part  
1610 of the line. The aliquots were subsequently evacuated to approximately  $10^{-10}$  mbar pressure.  
1611 The line was heated overnight at  $200^\circ\text{C}$  to remove all gases adsorbed on metal parts of the  
1612 line. Samples were, however, not heated, to avoid any  $^{40}\text{Ar}_{\text{rad}}$  removal. The reactor was  
1613 running several blank measurements to achieve signal of  $^{40}\text{Ar}$  lower than 0.01 V measured on  
1614 FAR detector (corresponding to 650000 cps on multiplier). Then, each sample was melted in  
1615 a double-vacuum resistant crucible at above  $1200^\circ\text{C}$  (assessed visually). CuO added to the  
1616 samples enhances oxidation of organic matter during this step. Titanium sponge (>99.99% Ti)  
1617 was always put to the place of the reactor (~0.5 g), where samples are heated. This was a first  
1618 cleaning level of gases extracted from the samples. Most of the cleanup was achieved when  
1619 temperature of the reactor was decreasing, which was monitored on Pirani gauge.

1620 Pure  $^{38}\text{Ar}$  produced by the Institute for Inorganic and Physical Chemistry of Bern  
1621 University was used as the spike. It was introduced to the extraction line after the sample  
1622 extraction using a calibrated pipette, built at Heidelberg University. Impurities of  $^{40}\text{Ar}$  and  
1623  $^{36}\text{Ar}$  in spike are regularly monitored and the final results are corrected for these impurities.  
1624 The final purification of argon was carried out in an isolated section of the line by a getter  
1625 pump (D-100, SAES Getters), previously baked overnight to remove excess argon. The  
1626 amount of gases poured to the spectrometer were optimized to keep  $^{40}\text{Ar}$  at level below 0.15  
1627 V, because otherwise fractionation on Nier ion source can occur (Kellett and Joyce, 2014).  
1628 Gas aliquot released from the sample was measured three times or more by opening and  
1629 closing valves of the line in a certain sequence.

1630 The amount of the original aliquot of  $^{38}\text{Ar}$  spike was determined by measuring  
1631 international standard GL-O (Odin, 1982:  $24.85 \pm 0.24 \cdot 10^{-6} \text{ cm}^3/\text{g STP } ^{40}\text{Ar}_{\text{rad}}$ ). This standard  
1632 is measured at least two times with every batch of the samples. Standard deviation of received  
1633 results for GL-O is  $\pm 0.09 (\pm 0.38\%) \cdot 10^{-6} \text{ cm}^3/\text{g STP } ^{40}\text{Ar}_{\text{rad}}$  for 19 measurements. Biotite LP-  
1634 6 was also tested for comparison (Odin, 1982:  $43.26 \pm 0.44 \cdot 10^{-6} \text{ cm}^3/\text{g STP } ^{40}\text{Ar}_{\text{rad}}$ ) and have  
1635  $43.08 \pm 0.41 (\pm 0.96\%) \cdot 10^{-6} \text{ cm}^3/\text{g STP } ^{40}\text{Ar}_{\text{rad}}$ . Every day, the  $^{40}\text{Ar}/^{36}\text{Ar}$  and  $^{40}\text{Ar}/^{38}\text{Ar}$  ratios  
1636 are measured for air sample aliquots, delivered from a calibrated air pipette. Based on this  
1637 results  $^{40}\text{Ar}/^{36}\text{Ar}$  and  $^{40}\text{Ar}/^{38}\text{Ar}$  ratios were corrected for instrument mass fractionation and  
1638 detector efficiencies assuming atmospheric ratios of  $(^{40}\text{Ar}/^{36}\text{Ar})_{\text{air}} = 298.57$  and  $(^{40}\text{Ar}/^{38}\text{Ar})_{\text{air}}$   
1639  $= 1583.5$  (Lee et al., 2006). The potassium contents were measured using Sherwood Model  
1640 420 flame photometer. The maximum error of this measurement was estimated to be equal  
1641 0.03% K. Based on 6 measurements, K content in GL-O glauconite was slightly higher:  $6.61$   
1642  $\pm 0.02\%$ , than that of standard:  $6.56 \pm 0.06\%$  (Odin, 1982). LP-6 biotite has slightly lower  
1643 amount of K:  $8.27 \pm 0.022\%$  (4 measurements) comparing to reference value:  $8.33 \pm 0.03\%$   
1644 (Odin, 1982). Both measured standards are within reference ranges assuming 0.03% K error.

1645 Age errors were calculated from the law of error propagation, taking into account  
1646 uncertainties of:  
1647 - spectrometric measurement of argon isotopes determined by spectrometer's software  
1648 delivered by Nu Instruments - sum of uncertainty for background and sample,  
1649 - weighting - assumed to be equal to  $\pm 0.03 \text{ mg}$ ,  
1650 - potassium measurements – equal to  $\pm 0.03 \%$  of absolute potassium content,  
1651 - normalization of amount of  $^{38}\text{Ar}$  in spike based on dating of GL-O standard – assumed to be  
1652 equal to  $\pm 0.4 \%$ ,  
1653 - assessment of  $^{40}\text{Ar}/^{36}\text{Ar}$  and  $^{40}\text{Ar}/^{38}\text{Ar}$  ratios, measured every day for air aliquots – equal to  
1654  $\pm 0.017 \%$  and  $\pm 0.013 \%$ , respectively.

### 1655 *Chemistry of the bulk rock and clay separates*

1656 Samples were ground in an agate mill and analyzed for the majority of elements at the  
1657 Bureau Veritas Mineral Laboratories (ACME) in Perth, Australia using a combo package,  
1658 which requires a single lithium borate fusion and provides major elements from X-Ray  
1659 Fluorescence (XRF) and trace elements (including REE) from Laser Ablation Inductively  
1660 Coupled Plasma Mass Spectrometry (LA-ICP-MS) on the same fused disc. Samples were pre  
1661 oxidized using 66:34 flux containing 10%  $\text{LiNO}_3$  in order to convert sulfides into sulfates. All

1662 elements were measured on the oven dry (105°C) weight basis. Loss on Ignition (LOI) was  
1663 determined from a separate 1g split using a Thermo Gravimetric Analysis (TGA) system with  
1664 furnaces set to 110 and 1000 °C. Boron content was measured by the Prompt-Gamma Neutron  
1665 Activation Analysis (PGNAA) with 0.5 ppm detection limit at the Activation Laboratories,  
1666 Canada.

#### 1667 *Mössbauer spectroscopy of the bulk rock and clay separates*

1668 The Mössbauer spectroscopy was used in order to quantify the oxidation state of iron  
1669 (recent review of the method applied to minerals in Murad, 2013). The Mössbauer spectra,  
1670 both for the bulk rock and for mineral separates, were recorded in the transmission geometry  
1671 at room temperature using a Wissel spectrometer. In addition, both fresh and hydrothermally  
1672 altered basalts were studied as reference. The samples were prepared in form of pellets, 12  
1673 mm in diameter, containing 100 mg specimen mixed with 200 mg lucide powder. The  
1674 velocity scale calibration was determined from  $\alpha$ -Fe foil standard.

1675 The spectra were evaluated with the use of *WinNormos-for-Igor* program. The spectra were  
1676 decomposed into sets of Zeeman sextets and quadrupole doublets. For each subspectrum the  
1677 hyperfine field  $B$ , isomer shift  $IS$  and quadrupole splitting  $QS$  were determined and used for  
1678 the identification of the iron bearing fractions. For natural mineralogical samples, due to the  
1679 distribution of the hyperfine parameters and overlapping of the subspectra, such identification  
1680 may be sometimes ambiguous. However, the distinction between  $Fe^{2+}$  and  $Fe^{3+}$  states is  
1681 obvious, due the significant difference in  $IS$ . The  $Fe^{2+}/Fe^{3+}$  ratio was determined as the area  
1682 ratio of the corresponding subspectra. The thickness saturation effects and differences in the  
1683 recoil free fraction of Fe in different states were not included into analysis. The typical  
1684 accuracy of the relative contribution of each component is 1%. The %  $Fe^{2+}$  values for clay  
1685 fractions are less accurate, in particular if abundant pyroxene is present.

#### 1686 *Fe isotopes of the bulk rock and clay separates*

1687 Fe isotope analyses ( $^{56}Fe/^{54}Fe$  and  $^{57}Fe/^{54}Fe$  ratios, reported as  $\delta^{56}Fe$  and  $\delta^{57/54}Fe$ ) were  
1688 performed for bulk rock samples and clay separates to trace possible microbial influence (cf.  
1689 Kappler et al., 2010). The measurements were conducted by ALS Scandinavia AB in Lulea,  
1690 Sweden, by MC-ICP-MS technique of Malinovsky et al. (2003).

#### 1691 *Oxygen isotopes*

1692 Oxygen isotopes were measured by Actlabs (Canada). Oxygen was extracted from 5 mg  
1693 samples at 550-600°C according to the conventional  $\text{BrF}_5$  procedure of Clayton and Mayeda  
1694 (1963) and analyzed via dual inlet on a Thermo-Finnigan DeltaPlusXP Isotope-Ratio Mass  
1695 Spectrometer (IRMS). The  $\delta^{18}\text{O}$  values are reported in permil (‰) relative to Vienna Standard  
1696 Mean Ocean Water (VSMOW), with a precision of about 0.1‰.

#### 1697 ***FTIR measurements***

1698 Middle infrared (MIR) investigations ( $4000 - 400 \text{ cm}^{-1}$ ) were performed in  
1699 transmission mode using a KBr beam-splitter and a DTGS/KBr detector on a Nicolet 6700  
1700 FTIR spectrometer. The spectra were obtained using KBr pressed pellets, 13 mm in diameter.  
1701 The pellets were prepared by mixing 1 mg of sample with 150 mg of well ground KBr. Then,  
1702 the mixture was pressed for 5 min at 5 kbars and 4 min at 12 kbars. The pellets thus prepared  
1703 were kept at 110 °C overnight in an oven before analyses. The spectra were recorded at  $4 \text{ cm}^{-1}$   
1704 resolution, from 100 co-added scans. Near infrared (NIR) spectra ( $7500 - 4000\text{-cm}^{-1}$ ) were  
1705 acquired with a Thermo-Scientific Integrating Sphere (diffuse reflectance) equipped with an  
1706 internal InGaAs detector, set on a Thermo-Scientific Nicolet 6700 FTIR spectrometer. A  
1707 white light source was used, associated with a  $\text{CaF}_2$  beam splitter. The resolution was set at 4  
1708  $\text{cm}^{-1}$  with the co-additions of 100 scans. Samples were analyzed directly on the integrating  
1709 sphere.

1710

#### 1711 ***Organic geochemistry***

1712

1713 Seven bulk rock samples (basalts or clays in basalt cavities: 4600-1, 4600-3A, 4600-  
1714 3B, and paleosols on basalts: 4504-3, 4504-4, 4504-5 and 4517-1) were used in the organic  
1715 geochemistry study. Total carbon (TC), total inorganic carbon (TIC), and total sulphur (TS)  
1716 contents were measured using an Eltra CS-500 IR-analyzer with a TIC module. TC was  
1717 determined using an infrared cell detector in  $\text{CO}_2$  gas evolved by combustion in an oxygen  
1718 atmosphere. TIC contents were derived from a reaction with hot 15% hydrochloric acid; the  
1719 resulting  $\text{CO}_2$  was determined using an infrared detector. Total organic carbon (TOC) was  
1720 calculated as the difference between TC and TIC. Calibration was made according to the Eltra  
1721 standards. The samples crushed to ca. 100 mesh were extracted using a dichloromethane  
1722 (DCM)-methanol mixture (1:1 v:v) with an accelerated Dionex ASE 350 solvent extractor.  
1723 Elemental sulphur was removed using an activated copper mesh. Due to low TOC values and

1724 low extract yields, samples were not separated into fractions. The *n*-hexane aliquots of the  
1725 total extracts were converted to trimethylsilyl derivatives via a reaction with N,O-bis-  
1726 (trimethylsilyl)trifluoroacetamide (BSTFA) and pyridine for 3 h at 70 °C. A blank sample  
1727 (silica gel) was analysed using the same procedure. Only trace amounts of phthalates and fatty  
1728 acids (FAs) were detected. All solvents were spectroscopically pure and the *n*-hexane for  
1729 derivatization was of super-dehydrated grade. The GC-MS analyses were carried out using an  
1730 Agilent Technologies 7890A gas chromatograph and an Agilent 5975C mass spectrometer  
1731 with a Triple-Axis Detector at the Faculty of Earth Sciences, Sosnowiec, Poland. Helium (6.0  
1732 Grade) was used as the carrier gas at a constant flow of 2.6 ml/min. Separation was performed  
1733 in either of two fused silica columns:

1734 (i) J&W HP5-MS (60 m × 0.32 mm i.d., 0.25 µm film thickness) coated with a chemically  
1735 120 bonded phase (5% phenyl, 95% methylsiloxane). The GC oven temperature was  
1736 programmed from 45 °C (1 min) to 100 °C at 20 °C/min, then to 300 °C (held for 60 min) at 3  
1737 °C/min. Solvent delay = 10 min.

1738 (ii) J&W DB35-MS (60 m × 0.25 mm i.d., 0.25 µm film thickness) coated with a chemically  
1739 bonded phase (35% phenyl, 65% methylsiloxane). The GC oven temperature was  
1740 programmed from 50 °C (1 min) to 120 °C at 20 °C/min, then to 300 °C (held for 60 min) at 3  
1741 °C/min. Solvent delay = 15 min. The GC column outlet was connected directly to the ion  
1742 source of the MSD. The GC-MS interface was at 280 °C, while the ion source and the  
1743 quadrupole analyser were at 230 and 150 °C, respectively. Spectra were recorded from *m/z*  
1744 45–550 (0–40 min) and *m/z* 50–700 (> 40 min). The mass spectrometer was operated in the  
1745 electron impact mode (ionisation energy 70 eV).

1746

### 1747 ***Petrographic observations***

1748

1749 Petrographic studies were performed on thin sections and rock fragments using a  
1750 polarizing optical microscope (Nikon Eclipse E600POL) and a JEOL IT 500 SEM equipped  
1751 with an EDS (BRUKER XFlash 4030 Silicon drift detector). SEM observations were  
1752 performed in secondary electron imaging mode (SEI) for morphological investigations and  
1753 backscattering electron mode (BSE) on carbon-coated thin sections for imaging of chemical  
1754 contrast and selection of local sites for punctual chemical analysis. Analytical conditions were  
1755 15 kV, 1 nA, a counting time of 60 s and a working distance of 16.5 mm. The standards used  
1756 for EDS consisted of albite (Na, Al, Si), almandine (Mg, Fe), diopside (Ca), orthoclase (K)  
1757 and spessartine (Mn). Matrix corrections were performed using integrated programs (a

1758 PhiRhoz correction). Reproducibility of the standard analyses was close to 1.5% for all of the  
1759 elements, except Na (3%).

1760 ***References***

1761 Clayton, R.N., Mayeda, T.K., 1963. The use of bromine pentafluoride in the extraction of  
1762 oxygen from oxides and silicates for isotopic analysis. *Geochimica et Cosmochimica Acta* 27,  
1763 43-52.

1764

1765 Jackson, M.L., 1975. *Soil Chemical Analysis – advanced Course*. 2nd edition, published by  
1766 the author, Madison, Wisconsin, 895 pp.

1767 Kappler, A., Johnson, C.M., Crosby, H.A., Beard, B.L., Newman, D.K., 2010. Evidence for  
1768 equilibrium iron isotope fractionation by nitrate-reducing iron(II)-oxidizing bacteria.  
1769 *Geochimica et Cosmochimica Acta* 74, 2826–2842.

1770 Kellet, D., Joyce N., 2014. Analytical details of single- and multicollection  $^{40}\text{Ar}/^{39}\text{Ar}$   
1771 measurements for conventional step-heating and total-fusion age calculation using the Nu  
1772 Noblesse at the Geological Survey of Canada. Geological Survey of Canada, Technical Note  
1773 8, 27 pp.

1774

1775 Lee, J.Y., Marti, K., Severinghaus, J.P., Kawamura, K., Yoo, H.S., Lee, J.B., & Kim, J.S.,  
1776 2006. A redetermination of the isotopic abundances of atmospheric Ar. *Geochimica et*  
1777 *Cosmochimica Acta* 70, 4507–4512.

1778

1779 Malinovsky, D., Stenberg, A., Rodushkin, I., Andren, H., Ingri, J., Ohlander, B., Baxte, D.C.,  
1780 2003. Performance of high resolution MC-ICP-MS for Fe isotope ratio measurements in  
1781 sedimentary geological materials. *Journal of Analytical Atomic Spectrometry* 18, 687–695.

1782 Moore, D.M., Reynolds Jr., R.C., 1997. X-ray Diffraction and the Identification and Analysis  
1783 of Clay Minerals. Oxford University Press, Oxford, 378 pp.

1784 Murad, E., 2013. Mossbauer Spectroscopy. In: Handbook of Clay Science, Bergaya, F.,  
1785 Lagaly, G. (Eds.), Elsevier, 11–24.  
1786

1787 Odin, G.S. and 35 Collaborators, 1982. Interlaboratory Standards for Dating  
1788 Purposes. In: Odin, G.S, ed., Numerical Dating in Stratigraphy. Wiley and  
1789 Sons, Chichester, 123-149.

1790 [Raven](#), M.D., Self, P.G., 2017. [Outcomes of 12 years of the Reynolds Cup quantitative](#)  
1791 [mineral analysis round robin](#). Clays and Clay Minerals 65, 122-134.

1792 Środoń, J., Drits, V.A., McCarty, D.K., Hsieh, J.C.C., Eberl, D.D., 2001. Quantitative X-ray  
1793 diffraction analysis of clay-bearing rocks from random preparations. Clays and Clay Minerals  
1794 49, 514–528.

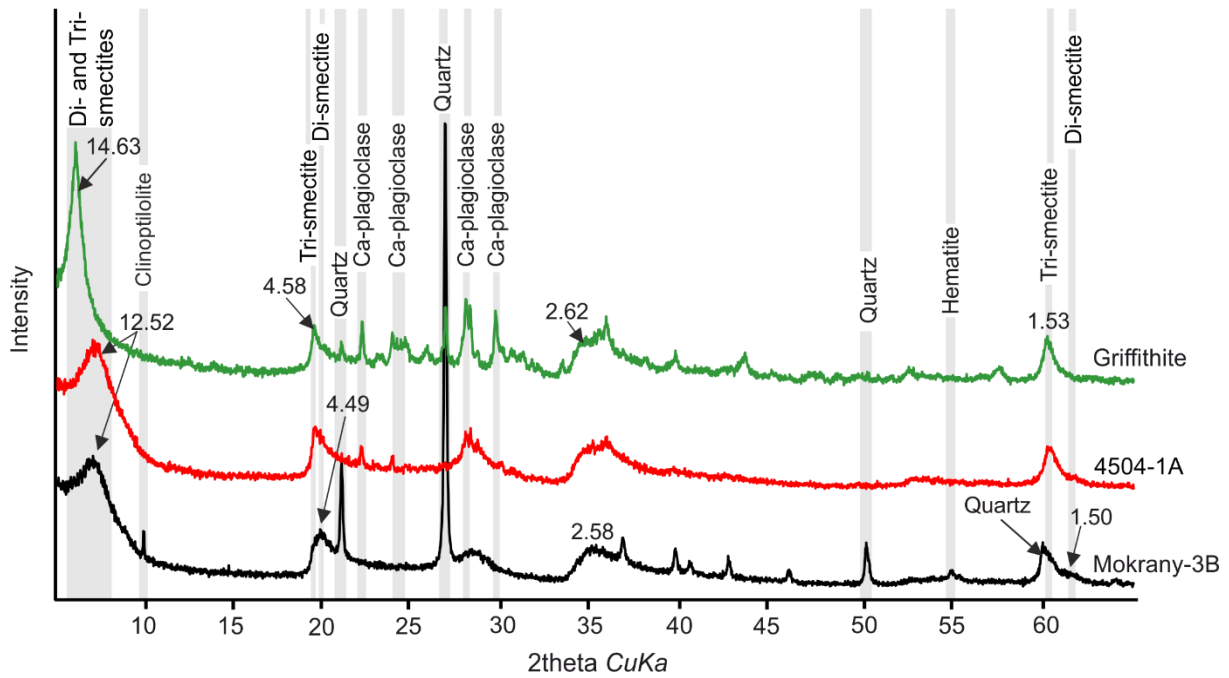
1795  
1796

1797 Inline Supplementary Figure 1. Random powder XRD patterns of the bulk rock, with ZnO  
1798 internal standard, illustrating the compositional variability of Volyn tuffs, from felsic (top) to  
1799 basic (bottom), with rhyodacite Skv-0C as reference.

1800



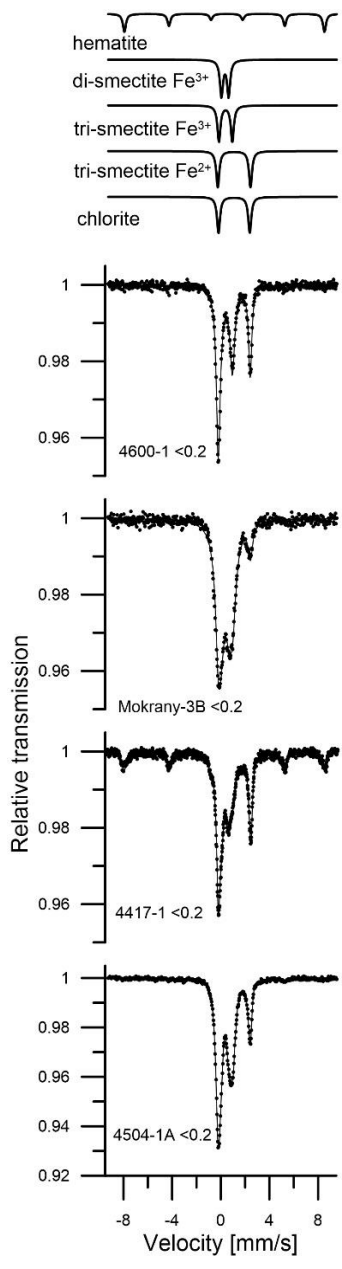
1810 Inline Supplementary Figure 3. Random powder XRD patterns of <0.2  $\mu\text{m}$  basalt clay  
 1811 fractions and <2  $\mu\text{m}$  fraction of griffithite, documenting coexistence of di- and trioctahedral  
 1812 smectite. The reference griffithite sample from Griffith Park, California, was provided by Dr.  
 1813 Jana Madejova.  
 1814



1815  
 1816  
 1817  
 1818

1819 Inline Supplementary Figure 4. Oriented glycolated XRD patterns of <0.2  $\mu\text{m}$  clay fractions,  
 1820 representative for the variability encountered in tuffs.





- 1830
- 1831
- 1832
- 1833
- 1834
- 1835
- 1836
- 1837
- 1838

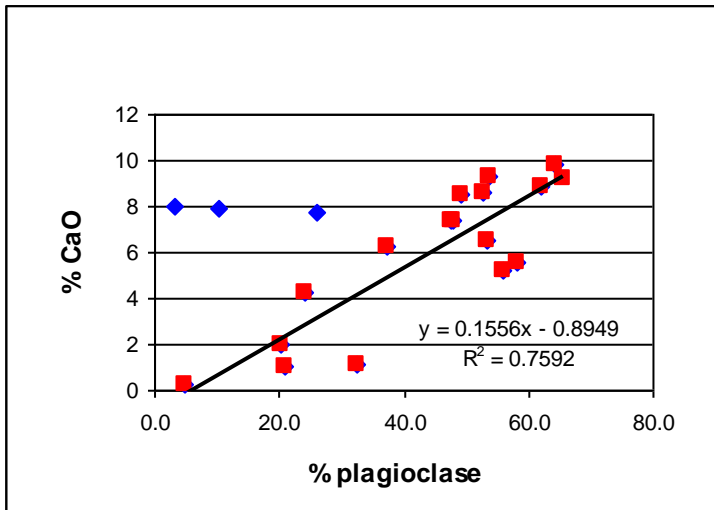
1839

1840 Inline Supplementary Figure 6. Relationship between % plagioclase from XRD and % CaO in

1841 basalts of variable degree of alteration. Three samples off the general trend (blue diamonds)

1842 contain calcite veinlets.

1843



1844

1845

1846

1847

1848

1849

1850

1851

1852

1853

1854

1855

1856

1857

1858

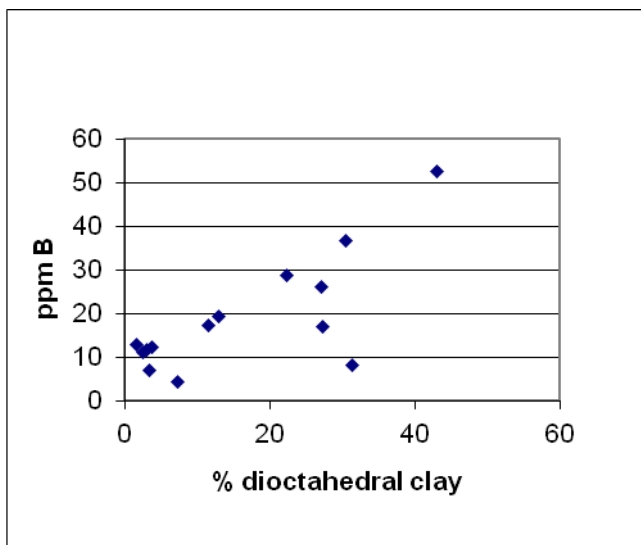
1859

1860

1861 Inline Supplementary Figure 7. Relationship between % dioctahedral clays from XRD and

1862 ppm boron in basalts of variable degree of alteration.

1863



1864

1865

1866

1867

1868

1869

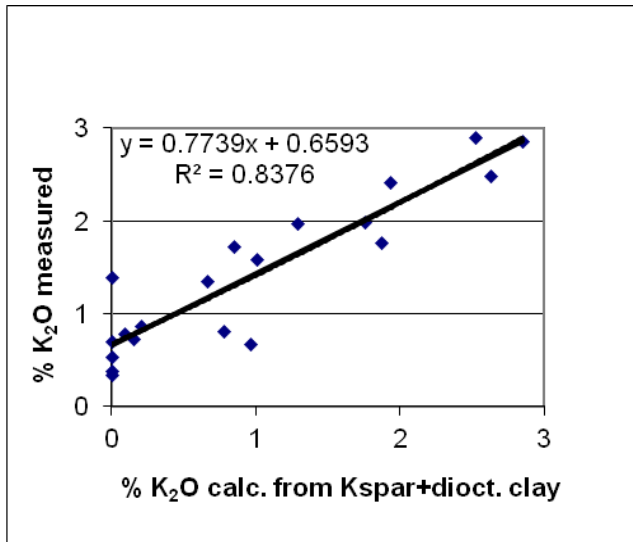
1870

1871 Inline Supplementary Figure 8. Relationship between %  $K_2O$  calculated from XRD contents

1872 of K-feldspar (assuming 12%  $K_2O$ ) and dioctahedral clay (6%  $K_2O$ ) and measured %  $K_2O$  in

1873 basalts of variable degree of alteration.

1874



1875

1876

1877

1878

1879

1880

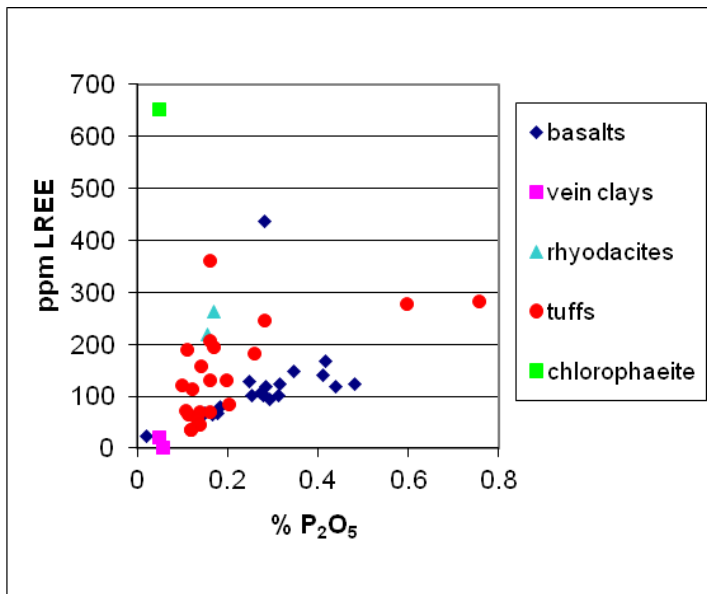
1881

1882

1883

1884 Inline Supplementary Figure 9. Relationship between % P<sub>2</sub>O<sub>5</sub> and ppm LREE in bulk rocks.

1885



1886

1887

1888

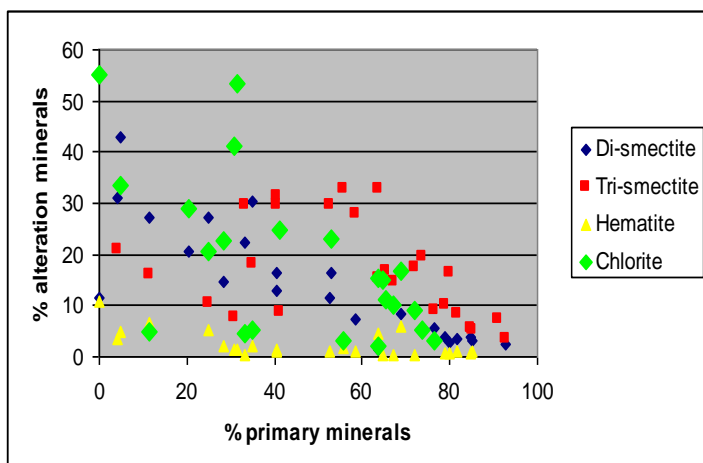
1889

1890 Inline Supplementary Figure 10. Quantitative evolution of secondary minerals in the course of  
 1891 basalt hydrothermal alteration(traced by percent of primary minerals).

1892

1893

1894



1895

1896

1897

1898

1899

1900

1901

1902

1903

1904

1905

1906

1907

1908

1909

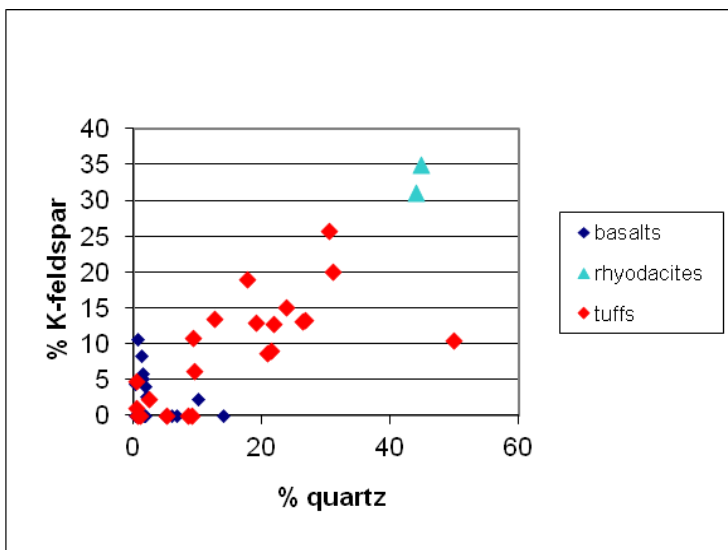
1910

1911

1912 Inline Supplementary Figure 11. Differentiation of tuffs into felsic (close to rhyodacite) and

1913 basaltic, based on quartz and K-feldspar XRD contents.

1914



1915

1916

1917

1918

1919

1920

1921

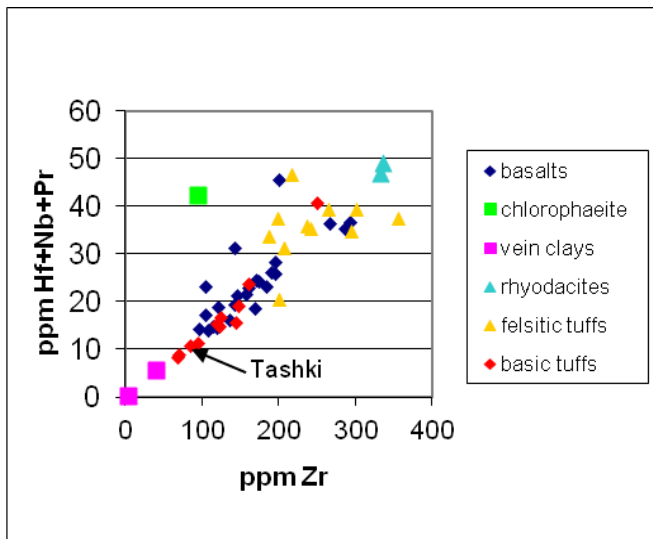
1922

1923 Inline Supplementary Figure 12. Chemical variability of tuffs (felsic vs. basaltic) traced using  
1924 the most immobile trace elements.

1925

1926

1927



1928

1929

1930

1931

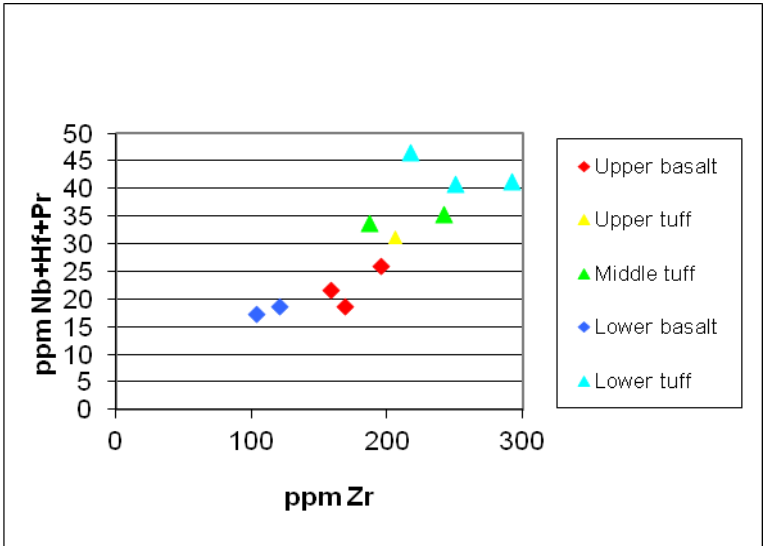
1932

1933

1934

1935 Inline Supplementary Figure 13. Chemical differences between basalts and tuffs illustrated  
1936 for a single profile (Kobryn) using the most immobile trace elements.

1937



1938

1939